Melt and fluid evolution in an upper-crustal magma reservoir, preserved by inclusions in juvenile clasts from the Kos Plateau Tuff, Aegean Arc, Greece

Author(s):
Fiedrich, Alina M.; Laurent, Oscar; Heinrich, Christoph A.; Bachmann, Olivier

Publication date:
2020-07-01

Permanent link:
https://doi.org/10.3929/ethz-b-000415263

Originally published in:
Geochimica et Cosmochimica Acta 280, https://doi.org/10.1016/j.gca.2020.03.038

Funding acknowledgement:
178928 - Dynamics of magma reservoirs in the earth's crust; focusing on the role of volatile elements (SNF)

Melt and fluid evolution in an upper-crustal magma reservoir, preserved by inclusions in juvenile clasts from the Kos Plateau Tuff, Aegean Arc, Greece

A.M. Fiedrich, O. Laurent, C.A. Heinrich, O. Bachmann

Abstract

Pre- to syn-eruptive fluids released by the magmatic system forming the non-welded rhyolitic Kos Plateau Tuff ignimbrite, Greece, were characterized using fluid inclusions entrapped in quartz from granitic clasts entrained from the roof or walls of the feeding magma reservoir. This fluid was initially of intermediate density and relatively low salinity (3-11 wt% $NaCl_{equivalent}$). Following significant pressure drop(s), it separated into immiscible brine and CO_2-bearing vapor occurring as texturally less mature inclusions. The transition from single- to two-phase-fluid occurred at magmatic conditions, as supported by high fluid inclusion homogenization temperatures (ca. 700 °C) and simultaneous trapping of fluid inclusions with silicate melt inclusions. The large recorded pressure drop together with texturally immature fluid inclusion shapes suggests a possible direct relation between the fluid phase change and the incipient 161 ka caldera-forming eruption. All inclusion types occur predominantly along (pseudo-) secondary trails in the granitic clasts, indicating efficient entrapment in microfractures formed at high crystallinity, as attested to by elevated concentrations of incompatible elements in the silicate melt inclusions.

Fast quenching of the inclusions due to eruption prevented significant post-entrapment chemical modification, providing pristine samples of magmatic fluid compositions. Element concentrations in co-existing fluids and silicate melt were analyzed using laser-ablation inductively-coupled plasma mass spectrometry and compared in view of element transporting capabilities and magmatic-hydrothermal ore formation. Economically important metals such as Cu, Zn, Mo, and W were extracted from the silicate melt by the fluid. In particular, Cu concentrations in the intermediate-density fluid in the range of 100-500 ppm agree well with previous experimental and modeling studies and, therefore, represent values expected for primary magmatic fluids. Most elements got further enriched in the brine upon phase separation, except Li, B, and As, which may have contributed significantly also to the vapor phase. Considering the similarity between vapor and intermediate-density fluid in terms of salinity, however, the metal-enriched brine phase only comprised a minor fraction of the bulk fluid.

1 Introduction

Magmatic-hydrothermal ore formation and different styles of volcanic eruptions both are interpreted as geological consequences of fluid saturation in upper crustal magma reservoirs (e.g., Burnham and Ohmoto, 1980; Cashman and Scheu, 2015, and references therein, Degruyter et al., 2017; Dilles, 1987; Holloway, 1981; Popa et al., 2019; Shinohara et al., 1995; Sillitoe, 1973; Wilson, 1976). The geological record of such fluids, however, is difficult to preserve in exposed systems and subject to questions. Near the surface, fluid saturation is expressed as bubbles in quenched volcanic material and in fumarolic fields above active magma reservoirs. Fluids reaching the surface as expanded gases are chemically modified and bear little resemblance with the denser fluids exsolved from magmas at greater depth. Since timing and conditions

of fluid exsolution are major parameters controlling the physico-chemical properties of magma reservoirs and the ore-forming capacity of fluids (e.g., Audétat, 2019; Cline and Bodnar, 1991; Veksler, 2004; Webster, 2004), pristine fluid samples from a range of pressures are desired for studying the magmatic-hydrothermal transition, i.e. the stage at which the hydrous silicate melt exsolves a magmatic volatile phase.

Fluid inclusions can provide samples of unmodified magmatic fluids, if they are well preserved. Characterizing such fluids is key to (1) determine the nature and entrapment conditions of primary exsolved fluids from magmas, (2) study element partitioning between fluids and melts in upper crustal silicic magma chambers, and (3) assess their control on the formation of magmatic-hydrothermal ore deposits above such magma reservoirs. Indeed, there are many reports of fluid inclusion chemistry from ore deposits (e.g., Klemm et al., 2007; Li et al., 2012; Rusk et al., 2008; Ulrich et al., 2002), as well as barren high-level granites containing miarolitic cavities, which represent local fluid pockets in highly crystallized magmas coexisiting with fractionated residual melt (e.g., Audétat and Pettke, 2003; Audétat et al., 2008; Zajacz et al., 2008; Zeng et al., 2016). However, post-entrapment modification by alteration and diffusive re-equilibration is now recognized as a serious obstruction to obtaining pristine compositions of fluid and silicate melt inclusions (SMI) at depth. This is especially true for fluid inclusions in and around ore deposits that precede the main hydrothermal stage (Bakker and Jansen, 1990; Hall and Sterner, 1995; Kamenetsky and Danyushevsky, 2005; Lerchbaumer and Audétat, 2012; Mavrogenes and Bodnar, 1994; Seo and Heinrich, 2013; Severs et al., 2007; Zajacz et al., 2009).

Inclusions from rapidly quenched and decompressed volcanic ejecta potentially offer the most pristine compositions of primary magmatic volatiles, if contained in host crystals strong enough to withstand fracturing during eruption. However, only few studies report the fluid inclusion record in volcanic deposits (Roedder and Coombs, 1967; De Vivo et al., 1995; Fulignati et al., 2001) because fluid inclusions in juvenile volcanics are rare. In addition, preserved inclusions are typically relatively small since quick decompression leads to physical decrepitation of larger inclusions. Therefore, characterizing primary magmatic fluids from magma reservoirs remains a challenge in linking the source of fluids and their metal-carrying capacity to the formation of magmatic-hydrothermal ore deposits. This study focuses on inclusions discovered in a large (> 60 km^3), non-welded ignimbrite from an active subduction zone, preserved thanks to the ejection of granite xenoliths interpreted to be co-magmatic with the eruptive system (e.g., Bachmann, 2010).

2 Geologic setting

2.1 Geodynamic background of the Kos-Nisyros volcanic system

The South Aegean Volcanic Arc (SAVA; Figure 1) is located at the margin of the ca. 30 km thick Aegean microplate (Sodoudi et al., 2006), which overrides the African plate at the Hellenic trench with a slow convergence rate of ca. 1 cm/yr (DeMets et al., 1990) and a mean subduction angle of ca. 25-30° (Papazachos and Comninakis, 1971; Papazachos et al., 2005). The Aegean region is undergoing extension at an average rate of ca. 3 cm/yr (e.g., Sodoudi et al., 2006). In addition, geophysical data imply that the African continental crust has reached the trench, slowing down subduction and decreasing magma production (Meier et al., 2004). Volcanism in the SAVA has been active for slightly less than 5 Ma (Francalanci et al., 2005).

The SAVA hosts five volcanic centers: Sousaki (also: Crommyonia), Aegina-Poros-Methana, Milos, Christiana-Santorini-Kolumbo, and the Kos-Nisyros-Yali volcanic system (KNYVS; Figure 1) in the very east (e.g., Francalanci et al., 2005; summarized in Vougioukalakis et al., 2019). Volcanism in the KNYVS was initiated by small eruptions of andesites and dacites a

few million years ago (e.g., Kefalos dacite dated at ca. 3 Ma; Bachmann et al., 2010a; Matsuda et al., 1999). It continued with more silicic (largely rhyolitic) volcanism, producing domes and minor pyroclastic deposits around 1 to 0.5 Ma on the Kefalos peninsula (Bachmann et al., 2010a, 2012; Francalanci et al., 2005, and references therein). Volcanic activity culminated in the caldera-forming Kos Plateau Tuff (KPT) eruption (Allen and Cas, 1998; Bachmann et al., 2019). After eruption of the KPT, volcanic activity shifted to the southern part of the caldera, building the volcanic islands of Nisyros and Yali (both younger than 160 ka).

Magmatism follows a typical calc-alkaline geochemical trend (Francalanci et al., 2005; Francalanci and Zellmer, 2019; Innocenti et al., 1981; Mitropolous et al., 1987) pointing to an important contribution of fluid flux melting of the mantle wedge. Magmatic evolution in the KNYVS is dominated by fractional crystallization of a mantle-derived mafic parent, with only minor crustal assimilation (e.g., Bachmann et al., 2010b, and references therein; Klaver et al., 2017). The products of the KNYVS are predominantly silicic (rhyolitic to rhyodacitic) in composition, and the establishment of an extensive caldera implies a large, upper crustal magma chamber (Nomikou et al., 2018) by the time of the eruption of the KPT and the Nisyros Lower and Upper Pumice. The KNYVS rests on sediments of the Lycian Nappes in the Cyclades-Menderes extensional province (e.g., van Hinsbergen and Boekhout, 2009). van Hinsbergen and Boekhout (2009) and Willmann (1983) provided a summary describing the various marine, limnic-fluviatile, and continental sedimentary rocks outcropping on Kos. Geothermal wells on Nisyros intersected shales and schists, limestones, marbles and skarns, and a dioritic intrusive body, beside variably hydrothermally altered and contact-metamorphosed igneous rocks (Italiana, 1983).

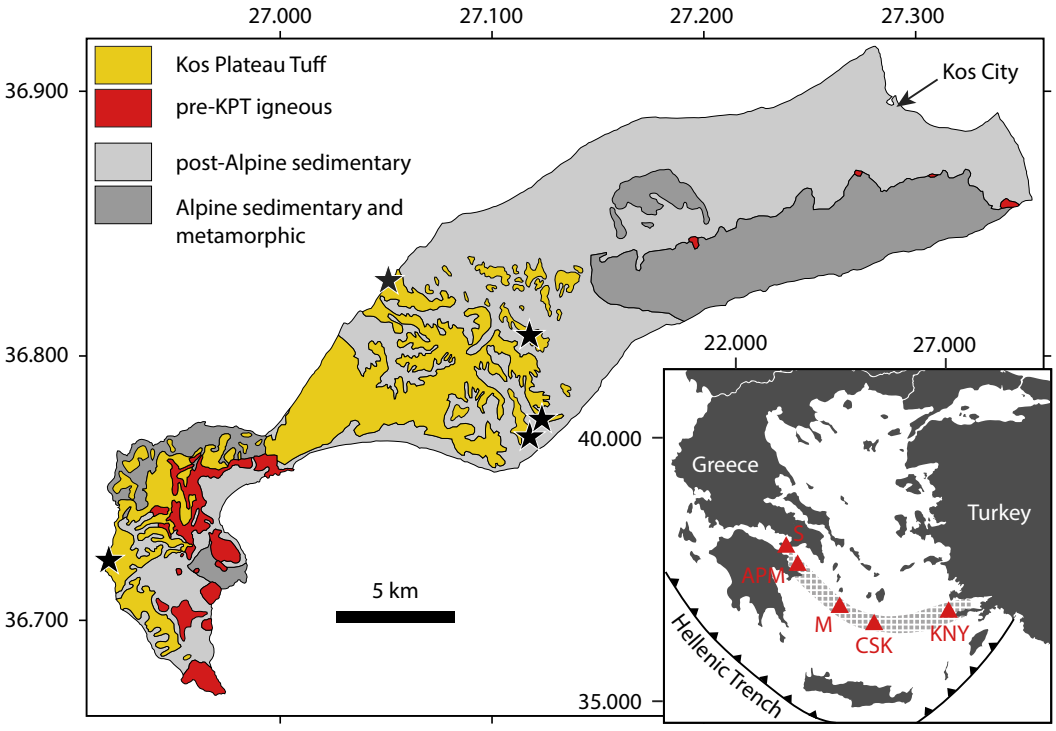

Figure 1: Geological map of Kos island, simplified and modified from Nomikou et al. (2018) and Nomikou (2004), and its location in the Aegean Sea (inset; label KNY = Kos-Nisyros-Yali). Stars represent sampling locations, the shaded area in the inset represents the South Aegean active volcanic arc. Volcanic centers indicated by red triangles, from west to east: Sousaki (S), Aegina-Poros-Methana (APM), Milos (M), Christiana-Santorini-Kolumbo (CSK), and Kos-Nisyros-Yali (KNY).

2.2 Eruption of the Kos Plateau Tuff

The largest Quaternary volcanic eruption of the SAVA produced the rhyolitic, ca. 161 ka KPT (Figure 1; Smith et al., 1996). An episode of mafic recharge most likely triggered this eruptive event (e.g., Bachmann et al., 2007; Piper et al., 2010), which released >60 km^3 of rhyolitic magma (Allen and Cas, 1998), depositing ash, pumice, and lithic clasts on Kos island and as far as the Turkish Datça peninsula and the surrounding Greek islands (Allen, 2001; Keller, 1969; Pe-Piper et al., 2005; Zouzias and St. Seymour, 2008).

The KPT displays ash-rich fall deposits at the base and top of the stratigraphic column (A, Ff), which bracket a series of internally stratified (B, C, Fs) and massive (D, E) pyroclastic density current deposits (Allen et al., 1999). The initiation of caldera collapse is represented by the basal lithic breccia of unit E (Allen, 2001; Allen and Cas, 1998), which features lithic clasts of up to 2 m in diameter. These include dominantly andesitic clasts and tuffs from volcanic edifices pre-dating the KPT eruption (Voegelin et al., 2014, and references therein) and co-magmatic granitic clasts (Bachmann et al., 2007; Keller, 1969). The latter clasts are the focus of the present SMI and fluid inclusion study. The eruption style changed from wet, phreatomagmatic to dry, magmatic volatile phase (MVP)-driven with increasing mass flux (Allen, 2001; Dufek and Bergantz, 2007).

Storage conditions of the magma at depth were estimated to be ca. 200 MPa and between 700-780 °C based on pumice samples, whereas granitic clasts (without glass) were stored at lower temperatures of 580-650 °C, both at an fO_2 of NNO+0.5 to +2 (Bachmann et al., 2007, 2010b; Bachmann, 2010; Keller, 1969). Fractionation of the mantle-derived, mafic parental magma followed a dominantly closed-system path with limited crustal assimilation as shown by homogeneous and mantle-dominated bulk-rock isotopic signatures (εNd = +0.2 to +1, $^{87}Sr/^{86}Sr$ = 0.7040 to 0.7045; Bachmann et al., 2007). Zircon U-Pb ages record a crystallization range of 160 to >300 kyr prior to eruption (Bachmann et al., 2007; Guillong et al., 2014), indicating a prolonged crystallization history within the subvolcanic magma reservoir.

2.3 Degassing of the Kos-Nisyros-Yali Volcanic System

Measurements of magmatic volatiles from fumaroles, soil diffusive degassing, etc. are common to study processes in the magma chamber beneath active volcanoes, but interpreting their signals remains challenging (e.g., Aiuppa et al., 2009; Edmonds, 2008; Fischer and Chiodini, 2015; Oppenheimer, 2003; Shinohara, 2008; Symonds et al., 2001). This is because the volatiles are overprinted on their ascent through the crust as they expand and react with the wall rock (e.g., Henley and Seward, 2018). Current degassing of volatiles in the KNYVS is monitored in view of potential hazards related to future eruptions, in particular phreatic explosions, and potential exploration for geothermal energy (Bini et al., 2019; Brombach et al., 2001; Caliro et al., 2005; Chiodini et al., 2002; Marini et al., 1993; Papadopoulos et al., 1998). Hydrothermal manifestations comprise fumaroles and hot springs, mostly located on Nisyros and Yali at present. Gases released by fumaroles mainly consist of H_2O, CO_2, and H_2S, but also some N_2, H_2, CH_4, CO, Ar, and He (Chiodini et al., 2002). Diffuse emission of hydrothermal CO_2 at Nisyros' Lakki plain, the present hydrothermal center of the KNYVS, amounts to 92 ± 8 tons/day (Bini et al., 2019). Evidence for a magmatic component is provided by isotopic compositions (δD, δ^{18}O, δ^{13}C, δ^{34}S) and noble gas ratios (Brombach et al., 2003). Fumaroles are fed from a boiling hydrothermal system rather than tracing back to a directly ascending magmatic volatile phase, as indicated, e.g., by the absence of strongly acidic gases (Chiodini et al., 1993). During and after periods of seismic unrest, chemical changes can be observed (Chiodini et al., 2002; Shimizu et al., 2005): The H_2S/CO_2 and $^3He/^4He$ ratios increase while the CH_4/CO_2 ratio decreases. These changes are likely related to an increasing input of magmatic gases, which in turn causes heating of the hydrothermal system and/or opening of new conduits

(Chiodini et al., 2002; Shimizu et al., 2005).

2.4 Pumice and co-genetic granitic clasts from the Kos Plateau Tuff

Both juvenile pumices (from different sub-units but focusing on unit E) and co-genetic granitic clasts (Bachmann, 2010; Keller, 1969) were studied for SMI and fluid inclusions. Pumices are: (a) non-welded and, therefore, offer excellent conditions for fast quenching and good preservation of inclusions, (b) rhyolitic in composition (71-76 wt% SiO_2; with 13-15 wt% Al_2O_3 and 7.4-7.9 wt% Na_2O + K_2O; Bachmann, 2010; Bachmann et al., 2007, 2010b), and (c) dominantly crystal-rich (ca. 25-35 vol%; Bachmann et al., 2007; Bouvet De Maisonneuve et al., 2009). The mineral assemblage comprises phenocrysts of quartz, sanidine, plagioclase, and biotite. In addition, accessory phases such as ilmenite, magnetite, apatite, zircon, and monazite are present (Bachmann et al., 2007). Most pumices exhibit tubular vesicles, but frothy, micro-vesicular, and compositionally mingled types also occur (Bachmann, 2010; Bouvet De Maisonneuve et al., 2009).

Centimetric to decimetric granitic blocks are present within the KPT (Keller, 1969; Appendix). Texturally, three subtypes can be distinguished: (1) equigranular coarse-grained, (2) porphyritic, and (3) fine-grained (Bachmann, 2010). They exhibit the same mineralogy and zircon crystallization age range as KPT pumices and are, therefore, assumed to have formed co-genetically (Bachmann, 2010; Bachmann et al., 2007; Keller, 1969). More specifically, they likely represent parts of the highly crystalline rind of the magma reservoir prior to the KPT eruption. Their very high crystallinity (0 to 20 vol% interstitial melt, now preserved as glass, which may be vesiculated; Keller, 1969) indicates an origin from the roof or walls of the magma chamber (Allen, 2001). An origin from melting of a pre-existing granite body, as initially proposed (Keller, 1969), is improbable according to the zircon age range and because re-melting of a sub-solidus magma body in the upper crust is thermally extremely challenging (e.g., Bachmann et al., 2002). However, the presence of corroded crystals (Keller, 1969), inverse zoning close to the crystal margin in plagioclase (Bachmann, 2010), and banded pumice (Allen, 2001) suggest some re-melting of the mush ("defrosting" or "mush reactivation"; Mahood, 1990; Parmigiani et al., 2014) by magma recharge. Co-genetic granitoids (often termed cognate xenoliths) have also been reported from other localities, such as the Taupo volcanic zone in New Zealand (Brown et al., 1998; Burt et al., 1998; Charlier et al., 2003) and Crater Lake in the USA (Bacon and Lowenstern, 2005).

All granitic clasts analyzed here are coarse-grained (>2 mm), equigranular with a few larger phenocrysts, and holocrystalline, i.e. contain no visible glass. Some of the sampled granite blocks are fragile and readily crumble when being handled. This is explained by an extensive network of cracks (and potentially vesiculated glass at the grain boundaries, if present at all), which formed during the explosive volcanic eruption. Granite blocks show very little primary porosity, but a number of small (<3 mm) cavities (Appendix), sometimes lined by euhedral crystals, indicate the presence of an exsolved volatile phase.

Silicate melt inclusions in quartz phenocrysts from KPT pumices and some granitic clasts were studied by Bachmann et al. (2010b). They found H_2O and CO_2 contents of around 4.5-6.5 wt% and 15-140 ppm, respectively, in glassy inclusions. This range is explained by variable entrapment pressures (crystals originating from variable depth in the erupted crystal mush) and potentially variable gas flux from depth (Bachmann et al., 2010b, and references therein).

3 Methodology

3.1 Field work and sample preparation

Samples for this study were collected during three field campaigns in 2004, 2005, and 2015. They consist of pumices and cogenetic granitic clasts included in the KPT. Sampling locations are indicated in Figure 1 and documented in Appendix A. Crystals were hand-picked from crushed samples. Thin sections of rock samples and doubly-polished thick sections of grain mounts were prepared for SMI and fluid inclusion studies at ETH Zurich.

3.2 Cathodoluminescence imaging

Panchromatic cathodoluminescence (CL) images of quartz crystals were acquired using an FEI Quanta 200F field emission gun (FEG) scanning electron microscope (SEM) at the Scientific Center for Optical and Electron Microscopy, ETH Zurich, and a JEOL JSM-6390 LA SEM at the Department of Earth Sciences, ETH Zurich. The Quanta is equipped with a Gatan MiniCL CL detector, and operation conditions were: 20 kV acceleration voltage and 21-22 mm working distance. The JEOL is equipped with a Deben Centaurus CL detector, and operation conditions were: 15 kV acceleration voltage and ca. 17 mm working distance.

3.3 Microthermometry

Temperatures of phase changes within fluid inclusions were recorded using a Linkam THMSG600 heating-freezing stage (up to ca. 540 °C) mounted onto a Nikon microscope stage. Calibration was performed using the triple point of CO_2 at -56.6 °C ± 0.2 °C, the final melting point of halite in a eutectic H_2O-NaCl solution at -21.2 °C ± 0.2 °C, the triple point (ice melting) of pure H_2O at 0.0 °C ± 0.1 °C, and the critical point of H_2O at 374.1 °C ± 2 °C, using synthetic fluid inclusions from Synflinc standards. Heating rates were 0.1-5 °C/min close to phase changes (slowest heating rates for ice and clathrate melting observations).

Total homogenization temperatures commonly exceeded the upper limit of the temperature range of the THMSG600 heating stage. Selected samples were studied using a Linkam TS1500 temperature-controlled microscopy stage (up to ca. 1100 °C) mounted onto a Leitz Orthoplan microscope stage. For these experiments, calibration was performed using the melting temperature of NaCl at 801 °C in addition to the critical point of pure water. Temperatures of phase transitions at high temperature may be slightly overestimated because external pressure was not applied and heating rates might have been faster than equilibration rates (Student and Bodnar, 1999).

Salinities, expressed as wt% $NaCl_{equivalent}$, were estimated from the dissolution temperature of halite in brine inclusions, from the final melting temperature of ice (freezing point depression) in intermediate-density (ID) fluid inclusions, and from clathrate melting temperatures in vapor inclusions (see Table 2 for description of inclusion types). Approximate salinities were calculated using the Excel spreadsheet Hokieflincs (Steele-MacInnis et al., 2012) for the system H_2O-NaCl for brine and ID fluid inclusions and the equations presented in Diamond (1992) for the system H_2O-CO_2-NaCl-KCl for vapor inclusions using the average K/Na ratio from LA-ICP-MS. Only fluid inclusion assemblages (Goldstein and Reynolds, 1994), and never single fluid inclusions, were targeted. Consequently, temperatures and salinities are reported as averages for each assemblage with 1σ uncertainty.

3.4 LA-ICP-MS microanalysis of quartz, silicate melt, and fluid inclusions

Laser-ablation inductively-coupled plasma mass spectrometry (LA-ICP-MS) was used for quantitative analysis of trace element concentrations in quartz and compositions of SMI and fluid inclusions (Günther et al., 1997; Heinrich et al., 2003; Pettke et al., 2012). All analyses were performed at the Department of Earth Sciences, ETH Zurich. The instrumental setup is described in Table 1. Samples, sample cell and transportation tubing were chosen and cleaned systematically using dilute HNO_3, following the recommendations of Schlöglova et al. (2017) to minimize contamination. Data reduction, including time-dependent instrumental drift, gas blank, and relative sensitivity corrections, was carried out with the MATLAB-based software SILLS (Guillong et al., 2008).

The method involves an inherent uncertainty that is difficult to estimate for each inclusion as it depends on ablation behavior and inclusion properties such as depth, size, and shape (Heinrich et al., 2003; Pettke et al., 2012). Potential sytematic erros (not estimated here) result from the choice of the internal standard (salinity estimate in the case of fluid inclusions) including the empirical salt correction (Heinrich et al., 2003). Analysis of Cl is challenging in inclusions other than brines because of the weak Cl signal, hindering comparison between different inclusion types. Therefore, representation of element concentration data relative to Na was preferred over absolute values.

Uncertainties were estimated for fluid inclusion assemblages by calculating the standard deviation of concentrations for the representative inclusion population, assuming that these represent a compositionally homogeneous fluid (e.g., Pettke et al., 2012). Averaging of several inclusions in an assemblage where some measurements fall below the limit of detection possibly leads to an overestimation of the concentrations for elements close to their detection limits (Helsel, 2012; Rauchenstein-Martinek et al., 2014; Schlöglova et al., 2017) because randomly higher signals are more likely to satisfy the detection criteria (statistically significant count rate above the background and clear signal discernible by inspection; Pettke et al., 2012). Nevertheless, assemblages with at least 50% of the inclusion data for any one element above the detection limit were used for interpretation.

In the case of ID fluid inclusions occurring together with silicate melt in the same assemblage, some inclusions contain heterogeneously entrapped fluid and melt. Such mixed inclusions contain random proportions of glass and fluid (Figure 3e,g,i) indicating trapping of random melt and fluid mixtures. They were, therefore, excluded from LA-ICP-MS analysis by optical identification as far as possible. However, accidental analysis of inclusions in which the glass was hardly identifiable was inevitable. These were then identified based on the Al signal, which when higher than that of the quartz indicated the presence of glass.

3.5 Electron probe micro-analysis of Cl, S, F in the silicate melt inclusions

For geochemical analysis using the SEM and electron probe micro-analyzer (EPMA), SMI in quartz were exposed at the surface, polished, and carbon coated. Homogenization of the inclusions was not required because they were fully glassy and did not show obvious signs of post-entrapment crystallization (i.e. the major element concentrations obtained by energy-dispersive x-ray spectroscopy (EDS) were in the expected range for rhyolitic melts and no daughter crystals were observed).

In a first step, standard-based major element analyses of SMI hosted in pumice quartz were performed using a JEOL JSM-6390 LA scanning electron microscope (SEM) equipped with a Thermo Fisher NORAN NSS7 EDS system with a 30 mm^2 silicon-drift detector, applying 15 kV acceleration voltage, 20 s counting time, ca. 2.5-3 nA beam current, and ca. 10 mm working distance. The resulting compositions of all analyzed SMI were averaged and subsequently

Table 1: Instrumentation and analysis parameters for LA-ICP-MS.

Analysis type	Trace elements in quartz	Silicate melt inclusions	Fluid inclusions
Laser ablation system			
Laser model and type	ASI (Resonetics) Resolution S-155; 193 nm wavelength	Coherent COMPex Pro 102F; 193 nm wavelength (Excimer ArF)	
Ablation cell	Laurin Technic dual volume S-155 cell, effective volume ca. 1 cm^3	In-house, fully glassy ablation cell, ca. 6 cm^3 volume	
Repetition rate	10 Hz for samples; 5 Hz for standards	10 Hz for samples; 5 Hz for standards	10 Hz
Spot diameter	29 μm	Variable for samples, set as to fully ablate the inclusion [a]; 20 μm for standards	Variable for samples, set as to fully ablate the inclusion [a]; 40 μm for standards
Energy density	ca. 5-7 J·cm^{-2} for standards and plagioclase, ca. 20-25 J·cm^{-2} for quartz		
Ablation duration	30 s	Dependent on inclusion depth for samples; 30-40 s for standards	Dependent on inclusion depth for samples; 30-40 s for standards
ICP-MS instrument			
Mass spectrometer model and type	Thermo Element XR sector field single-collector ICP-MS		Perkin Elmer NexION 2000 quadrupole ICP-MS
RF power	1375 W	1400-1600 W	1550 W
Detection system	Triple (pulse counting, analog, Faraday – calibrated daily)		Dual (pulse counting, analog – calibrated monthly)
Carrier gas flow (He)	0.5 L/min	0.9-1.2 L/min	0.9-1.2 L/min
Auxiliary gas flow (Ar)	0.85-1.0 L/min	0.92-1.0 L/min	0.9-1.125 L/min
Sample gas flow (Ar)	0.8-1.0 L/min	0.9-1.0 L/min	0.94-1.05 L/min
Masses measured	Li7, Al27, Si29, P31, Ca43, Ti49, Mn55, Ga69, Ga71, Ge72, Ge73	Li7, Be9, B11, Na23, Mg25, Al27, Si29, P31, K39, Ca43, Sc45, Ti49, Mn55, Cu63, Zn66, As75, Rb85, Sr88, Y89, Zr90, Nb93, Mo95, Sn118, Sb121, Cs133, Ba137, La139, Ce140, Pr141, Nd146, Sm147, Eu153, Gd157, Tb159, Dy163, Ho165, Er166, Tm169, Yb173, Lu175, Hf178, Ta181, W182, Pb208, Bi209, Th232, U238, (S34, Cl35, V51, Cr53, Co59, Ni62, Ag107 – usually below detection limit, only analyzed in the first runs)	Li7, Be9, B11, Na23, Mg25, Al27, Si29, P31, S34, Cl35, K39, Ca43, Mn55, Fe57, Cu63, Zn66, As75, Br79, Rb85, Sr88, Zr90, Mo95, Ag107, Sn118, Sb121, Cs133, Ba137, La139, Ce140, W182, Tl205, Pb20, Bi209, U238
Oxide formation rate (ThO^+/Th^+)	ca. 0.15 %	$\leq$ 0.5%	$\leq$ 0.5%
Dwell times	40 ms for Li, Ti, Ga, Ge; 11 ms for all others	5-25 ms	1-5 ms
Total sweep time	579 ms	635-707 ms [b]	40-135 ms [b]
Data processing			
Software	SILLS v.1.3.4 (Guillong et al., 2008)		
Gas blank	30 s	ca. 30 s	ca. 30 s
External standard	NIST SRM 612 [c]	NIST SRM 610 [c]	NIST SRM 610 [c], SCA17 [d]
Secondary reference materials	GSD-1G [e], smoky quartz [f]	GSE-1G [e]	-
Internal standard	99.9 wt% SiO_2	12.5 wt% Al_2O_3 and 100 wt% total oxides (quartz); 4.4 wt% K_2O (based on SEM-EDS analysis) and matrix-only tracer Ca43 (plagioclase)	inclusion salinity from micro-thermometry; empirical salt correction [g]

[a] using an adjustable iris aperture to avoid quartz cracking;
[b] depending on the used dwell times;
[c] Jochum et al. (2011);
[b] for S, Cl, and Br only, Seo et al. (2011);
[c] Guillong et al. (2007);
[d] Audétat et al. (2015);
[e] Heinrich et al. (2003)

entered in Probe for EPMA for matrix correction of EPMA analyses. Where possible (i.e. large enough inclusions), the samples were repolished before EPMA analysis to remove the potentially beam damaged surface layer, and recoated.

Analysis of Cl, S, and F was performed using a JEOL JXA-8200 EPMA with five wavelength-dispersive spectrometers and employing the software Probe for EPMA. To avoid element migration in the glass under the electron beam (e.g., Humphreys et al., 2006, and references therein; Varshneya et al., 1966), the beam current was reduced to 5 nA at a beam diameter of 2-5 μm (depending on the inclusion size) and a peak counting time of 60 s. In addition, a time-dependent intensity correction using Probe for EPMA was tested for the elements S, Cl, F, (Si, Al) but not applied in most cases because such time-dependent trends were not observed. The Na concentration was fixed to 4 wt% (based on the previously determined average from SEM-EDS analysis), as the values measured by EPMA indicated significant diffusion. Background counting time was avoided through a mean atomic number background correction (Donovan and Tingle, 1996; Donovan et al., 2016). For inclusions in granites, major elements were also analyzed by EPMA (Si and K on PETJ, Al and Na on TAPH; 20 s counting time each) to perform the matrix correction. Fluorine was standardized with F-phlogopite and analyzed using an LDE1 spectrometer, S with anhydrite or barite using a PETH (and PETJ for pumice SMI) spectrometer, and Cl with scapolite using a PETH spectrometer.

4 Results

4.1 Cathodoluminescence patterns and trace element geochemistry of quartz

Quartz crystals from six pumices and five granitic clasts were studied for their zoning patterns with CL imaging (Figure 2a). Subsequent trace element analysis of the different zones in quartz by LA-ICP-MS (Figure 2b-c) was used to characterize storage temperatures in the magma chamber and potential differences between pumice- and granite-hosted quartz. Pumice samples KPT04-2, -5, and -21 are derived from units B, D, and E, respectively. The first is a crystal-poor pumice, the other regular crystal-rich pumices. Granite samples NIS-U39, NIS-Andi, NIS37, and KPT04-20 all are holocrystalline. The dominant mineralogy consists of quartz, feldspars, and biotite. Only in sample NIS-U39, minor amphibole, clinopyroxene and some titanite were observed.

Quartz crystals from pumice and granitic clasts do not exhibit any striking differences in internal structures as revealed by CL imaging (Figure 2a). Both are dominated by oscillatory zoning. Patchy, cloudy patterns or homogeneous, unzoned crystals are rare. Resorption is recorded in many crystals through truncated oscillatory zoning. Silicate melt inclusions appear dark in CL images and, in some pumice-derived quartz, are associated with the margins of resorbed zones. Fluid inclusion assemblages cross-cut the oscillatory zoning visible in CL, and are not accompanied by a selvage of quartz of significantly different CL brightness.

Titanium concentrations are commonly used as a proxy for magma temperature (e.g., Wark and Watson, 2006) and hydrothermal quartz crystallization regime (e.g., porphyry vs. epithermal; Rusk, 2012). Here, all analyzed pumice samples and most of the granite samples cluster tightly around 50-80 ppm Ti (with a tendency toward the lower end for granites) and 60-100 ppm Al. This Ti concentration range is typical for late-magmatic temperatures and translates into ca. 760-700 °C (assuming $aTiO_2 = 0.6$ and P = 200 MPa; Huang and Audétat, 2012). CL-bright zones present in some crystals (Figure 2a), commonly correlate with elevated Ti and Al concentrations (79-91 ppm Ti and 97-109 ppm Al).

Lithium concentrations (Figure 2c) in quartz from pumice cluster around 3-5 ppm, with the exception of one sample (KPT04-5), which plots in the range of most granite samples around

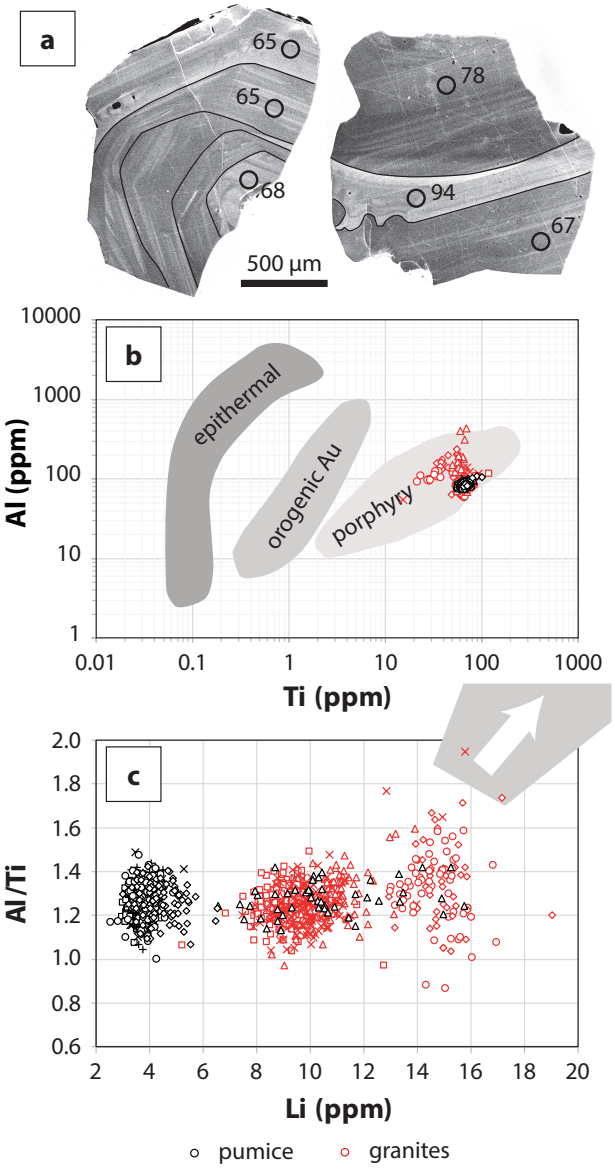

Figure 2: Trace element concentrations in quartz. (a) CL images of quartz crystals from pumice (left) and granite (right). Both crystals show concentric zoning, with resorption between broader zones. Circles indicate LA-ICP-MS analysis spots with corresponding Ti concentrations in ppm. While the crystal on the left has fairly homogeneous trace element concentrations, the one on the right has a CL-bright zone of elevated Ti (and Al) concentration. (b) Diagram of Al vs. Ti. All analyzed pumice samples and most of the granite samples cluster tightly. Only some quartz from granites plots outside this field. Gray fields represent the classification of Rusk (2012). (c) Diagram of Al/Ti vs. Li, allowing for distinction of different groups based on Li concentrations. The arrow points toward some even higher Li concentrations (up to ca. 35 ppm) and Al/Ti ratios (up to ca. 7) encountered in quartz from granitic clasts, which are not plotted here for better visibility of the more commonly found concentrations. Black symbols for samples from pumice: triangle = KPT04-24 (unit E), diamond = KPT04-9 (unit E), cross = KPT04-21 (unit E), circle = KPT04-6 (unit D/E), cross = KPT04-5 (unit D), square = KPT04-2 (unit B); Red symbols for samples from granite: circle = NIS-U39, triangle = KPT04-8, diamond = NIS37, square = KPT04-20, cross = KPT05-4.

8-11 ppm Li. Two granite samples (NIS37 and NIS-U39) show even higher Li concentrations around 13-16 ppm and a more variable Al/Ti ratio. As indicated by the arrow, some quartz from granitic clasts has even higher Li concentrations (up to 35 ppm) together with a higher Al/Ti ratio (up to 7).

Concentration ranges of Ti, Al, and Li (as well as Ge, not plotted here) in quartz are overall very narrow, but some of the quartz from granites shows anomalously high Al and Li concentrations (Figure 2b-c): These anomalies are neither linked to specific zones visible in CL images nor to inclusions, but characterize entire quartz crystals (several spots were analyzed on each quartz crystal).

4.2 Occurrence and microthermometric properties of fluid and silicate melt inclusions in the KPT

The magmatic-hydrothermal evolution from intermediate to low crystallinity was investigated using pumice and co-genetic granite samples (sampling locations in Figure 1). In contrast to pumice, quartz from granitic clasts contains abundant fluid inclusions in addition to SMI. The

Table 2: Overview over the fluid inclusion types in the KPT granitic clasts.

Inclusion type	Phases	Shape	Salinity	Homogenization behavior	Occurrence
Brine	usually 1-2 salt crystals (halite and sylvite), sometimes 1 birefringent crystal and/or small other crystal(s)*; liquid, bubble	well-rounded, elongate to irregularly shaped	ca. 34-50 wt% $NaCl_{eq.}$**	by bubble disappearance, to the liquid between 584 ± 4 °C and 700 ± 14 °C, with most assemblages around 680-690 °C	NIS-U39, NIS37
Vapor	ca. 70-90 vol% vapor, 10-30 vol% liquid; develop clathrate upon cooling, most show CO_2 double bubble that homogenized at or below room temperature	usually elongate to irregularly shaped	ca. 1-9 wt% $NaCl_{eq.}$	to the vapor at Th >330 °C (true Th invisible)	NIS-U39, NIS37, KPT04-20
Inter-mediate-density fluid	ca. 50-60 vol% vapor, 40-50 vol% liquid; salinity determined from ice melting, although some appear to contain CO_2 according to Raman	usually well-rounded or approximating negative crystal shape	ca. 3-11 wt% $NaCl_{eq.}$***; average and median ca. 6 wt%	critical homogenization (or to the vapor, not recorded) between 398 ± 3 °C and 438 ± 42 °C	NIS-U39, NIS37, KPT04-20, NIS-Andi

Error on temperature estimates represented by 2σ, if it exceeds the precision of the temperature reading of ca. ± 3 °C.

* The birefringent, transparent, colorless crystal is not Raman active and, thus, likely a complex salt. Upon heating, it melts before sylvite and halite. Small crystals present in some assemblages / single inclusions could be a third salt (e.g., colorless Mn-chloride) or opaque oxides. Observation of its dissolution temperature is usually very difficult; opaque crystals may not dissolve before halite.

** Tendency toward lower salinity of brines (ca. 34-43 wt% $NaCl_{equivalent}$) in NIS37 compared to NIS-U39.

*** Rare high-density vapor inclusion assemblages ("VL" in Figure 3j) with higher salinity (ca. 14-21 wt% $NaCl_{equivalent}$ were observed in NIS-U39).

selected samples differ in their fluid inclusion record, as outlined in Table 2 and detailed in Appendix A.

Silicate melt inclusions are abundant in quartz and plagioclase from both pumice and granitic clasts (Figure 3a-g), but interpretations are exclusively based on quartz-hosted inclusions (because of the physically strong crystal lattice without cleavage and the simple composition of quartz). Silicate melt inclusions in quartz from granitic clasts are dominantly (pseudo-) secondary (Figure 3e and g), typically forming trails and groups that do not follow crystal zoning. Primary SMI are more abundant in quartz from pumices (Figure 3a). In plagioclase from granitic clasts, on the other hand, both primary and secondary SMI assemblages are common (Figure 3d). On average, SMI in quartz from pumice are larger (often >50 μm) than those in quartz from granitic clasts (typically <20 μm; compare, e.g., Figures 3a and e). The analyzed SMI were texturally well equilibrated and exclusively completely glassy, although a variety of textures including necking and decrepitated inclusions exists (Figure 3b and c).

Three different types of fluids beside silicate melt were observed as inclusions in quartz in granitic clasts (Table 2): (a) ID fluid, characterized by a liquid phase and a vapor bubble of similar proportions at room temperature, (b) CO_2-bearing vapor, characterized by a larger proportion of vapor to liquid at room temperature and homogenization to the vapor phase, and (c) multiphase brines, characterized by liquid, a small vapor bubble, and one or several crystals at room temperature. The fluid inclusion assemblages predominantly occur as texturally coherent trails along healed fractures of the crystals and commonly terminate at the edge of the crystal. Therefore, they are termed secondary inclusion assemblages (Roedder, 1984). Many vapor and brine inclusions are unusually irregular in shape (Figures 3h and 5) despite the high entrapment temperatures (see following section) and consistent microthermometric properties (in any one assemblage) they record (Table 2), whereas ID fluid inclusions are generally more equant. No fluid inclusions of any type were observed in quartz from pumice.

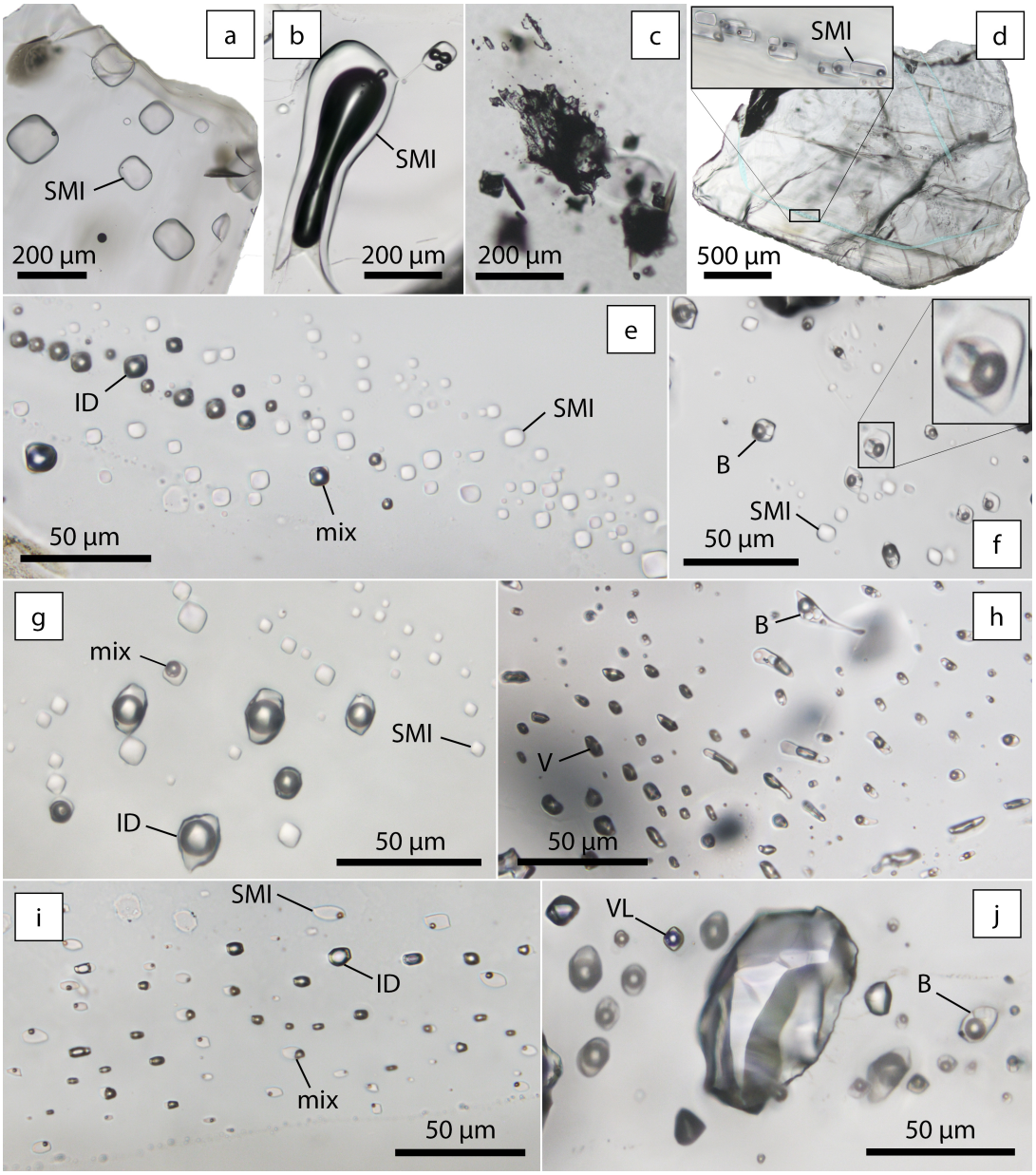

Figure 3: (a) Large, glassy SMI in quartz from sample KPT04-2 (pumice, unit B), some with small bubble; black dot from LA-ICP-MS analysis. (b) Doubly-necking glassy SMI with several dark bubbles at the crystal margin of quartz in sample KPT04-9 (pumice, unit E). (c) Irregular shape and dark interior points to decrepitation (explosion) of these quartz-hosted inclusions from sample KPT05-4 (granite, unit E). Smaller inclusions are more likely to be preserved. (d) Primary (following crystal zoning) and secondary (crossing crystal zoning) SMI trails, some of which are highlighted in light blue, in plagioclase of sample KPT04-21 (pumice, unit E). The enhanced image shows the elongate shape of and the bubble within the otherwise glassy, crowded primary inclusion assemblage. (e-i) Petrographic evidence for immiscibility between different phases. (e) SMI and ID fluid inclusions in quartz from sample NIS-Andi. A few heterogeneously entrapped inclusions (mix) occur. (g) SMI and ID in quartz from sample NIS37. (i) SMI, ID fluid, and heterogeneously entrapped (mix) inclusions in alkali feldspar from sample NIS37. Note that, similar to (d), the SMI contain a small bubble. (f) SMI and brine (B), with enhanced inclusion showing heterogenerous entrapment of both phases, in quartz from sample NIS-U39. (h) Brine (B) and vapor (V), again with some heterogeneously entrapped fluid between the two end-members, in quartz of sample NIS37. (j) High-salinity vapor with large liquid proportion (VL) and brine were also observed together, commonly near large, decrepitated inclusions (compare to Lowenstern, 1995), in quartz from sample NIS-U39.

Intermediate-density fluid inclusions in coherent assemblages were found in co-existence with SMI (Figure 3e,g,i). Furthermore, vapor and brine commonly were co-trapped in boiling trails (Figure 3h). Assemblages of co-existing brine and silicate melt (Figure 3f) as well as brine and vapor inclusions with a high liquid-to-vapor ratio approaching ID fluid inclusions (Figure 3j) are rare. The latter inclusions were typically observed in the vicinity of very large, decrepitated inclusions (Figure 3j) and contain significantly higher-than-average salinity (ca. 14-21 wt% $NaCl_{equivalent}$) and some CO_2, which could only be detected using Raman spectroscopy.

4.3 Entrapment conditions of KPT fluids

Temperatures of phase changes within the inclusions obtained by microthermometry were used to estimate salinities and entrapment conditions. The salinities and homogenization temperatures of the three observed fluid types are summarized in Table 2 (see also Figure 4). Brines were found to homogenize to the liquid phase by bubble disappearance, predominantly around ca. 680-690 °C. For those brines co-existing with vapor inclusions in the same assemblage (i.e. boiling trails), the observed homogenization temperature (T_h) corresponds to the entrapment temperature (Roedder, 1984), and the corresponding pressure estimated from the NaCl-H_2O model system is ca. 100-110 MPa (Figure 4a). In contrast, a pressure correction had to be applied to the homogenization temperatures (T_h) of ID fluid inclusions. If the calculated isochores of the ID fluid inclusions are intersected with the water-saturated haplogranite solidus (e.g., Audétat and Pettke, 2003; Johannes and Holtz, 1996), a temperature of ca. 680-690 °C at a pressure of up to ca. 180 MPa can be estimated. These higher pressures are closer to published estimates based on the composition of KPT glass and volatile saturation pressures of SMI in quartz phenocrysts (Bachmann et al., 2010b; Keller, 1969).

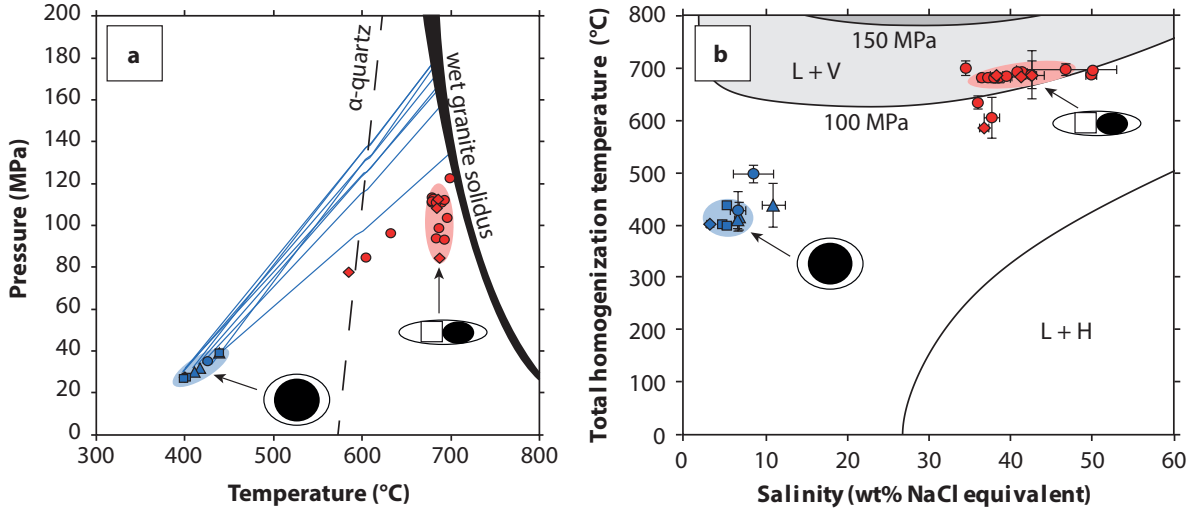

Figure 4: (a) Plot of pressure vs. temperature of selected inclusion assemblages at the point of total homogenization. The program SoWat (Driesner, 2007) was used to calculate pressures of brine inclusion assemblages (red); The FLUIDS package (Bakker, 2003) was used to calculate pressures and isochores (lines of constant volume) of ID (blue) inclusion assemblages. (b) Plot of total homogenization temperature vs. salinity as determined from microthermometry for some selected inclusion assemblages. The liquid-halite surface (L+H) and two isobaric sections of the liquid-vapor surface (L+V) in the system H_2O-NaCl were plotted using the program SoWat (Driesner, 2007). Error bars correspond to 2σ uncertainty. Symbols correspond to different samples: circle = NIS-U39, triangle = NIS-Andi, diamond = NIS37, square = KPT04-20.

A rare assemblage of co-existing brine and vapor on a single fracture is shown in Figure 5: Between smaller, more equant brine inclusions with 1-2 salt crystals and ca. 40 wt% $NaCl_{equivalent}$ (zone a; inset) and larger, highly irregularly-shaped and more interconnected vapor (zone c), there is a zone of irregularly shaped brine inclusions with additional crystals (one of which is distinctly birefringent) and significantly higher salinity (ca. 50 wt% $NaCl_{equivalent}$; zone b). Homogenization by bubble disappearance occurs at ca. 695 ± 10 °C for brines in both zones a and b (for typical homogenization temperatures in brines see also Figure 4). In the same sample (NIS-U39), brine-only trails with salinities around 40 wt% are very common, while brine-only trails with significantly higher salinities are rare.

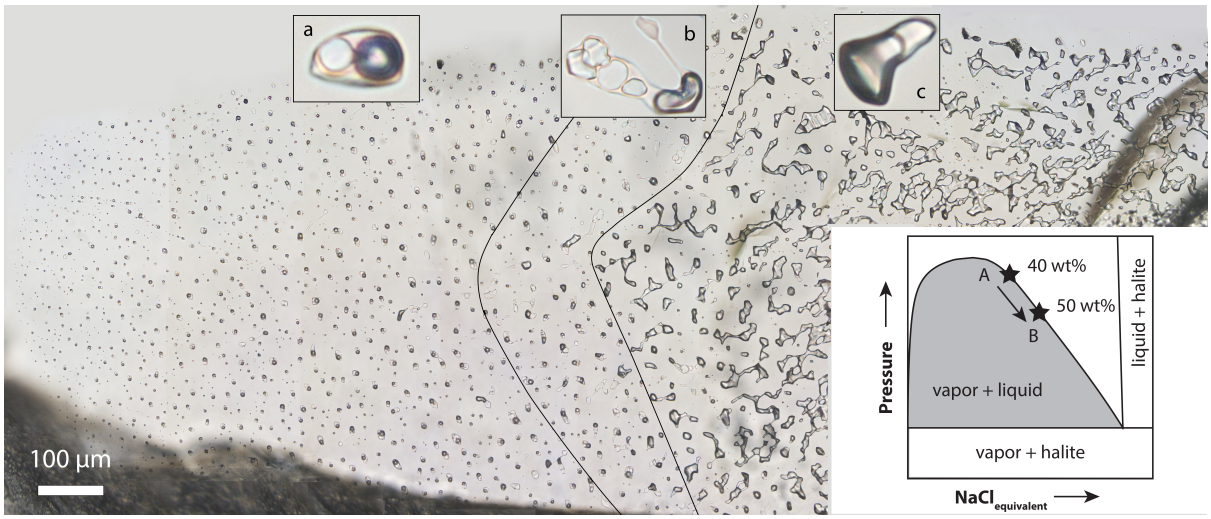

Figure 5: Unusually poorly healed inclusion trail of brine with ca. 41 wt% $NaCl_{equivalent}$ on the left (zone a), vapor-like fluid on the right (zone c), and brine with ca. 50 wt% $NaCl_{equivalent}$ in between (zone b). Black lines roughly separate the three zones of inclusions. This trail likely records the instant of further phase separation within a single microcrack, of a fluid that already was in or near the two-phase state. Sketch of isothermal slice of NaCl-pressure diagram exemplifies how further decompression leads to an increase in the salinity of the brine. Brine inclusions in zones a and b show the same range of homogenization temperatures between ca. 690-700 °C.

4.4 Compositional variations in silicate melt inclusion assemblages

Silicate melt inclusions in quartz were previously studied by Bachmann et al. (2010b). Results indicated that: (a) The SMI overlap in major and trace element composition with matrix glass of pumice. (b) They contain ca. 77-78 wt% SiO_2, making them slightly more evolved than the bulk pumice, which contains ca. 74-76 wt% SiO_2. Notably, high $Na_2O + K_2O$ concentrations of mostly >8 wt% indicate that post-entrapment loss of alkali elements from SMI was insignificant. (c) H_2O concentrations range between 4.25-7 wt% (measured by SIMS, Raman, and FTIR spectroscopy). No correlation between H_2O content and bubbles or fractures or between H_2O content and trace element concentrations was found (Bachmann et al., 2010b).

All SMI assemblages analyzed here are high-silica rhyolitic in composition, confirming the observations of Bachmann et al. (2010b). Silicate melt inclusion assemblages in pumice are relatively homogeneous in major and trace element composition (Figure 6a-c), and the compositions of quartz-hosted and plagioclase-hosted inclusion assemblages from pumice overlap (Figure 6b and c). In contrast, quartz-hosted SMI in granitic clasts show great variability in trace element concentrations (Figure 6a and d). While the SMI from pumice show a restricted range of REE concentrations and a mildly negative Eu anomaly, those from granitic clasts show

considerably more scatter (>1 order of magnitude), lower LREE/HREE ratios and range to deeper Eu anomalies (Eu commonly below detection limit; Figure 6a).

Granite-hosted SMI show clear correlations among trace elements: Cs, Mo, and Rb are positively correlated with each other (Figure 6d) and with B, As, Mo, Sn, Sb, W, Bi (not displayed here) and negatively correlated with Sr (Figure 6d) and Ba (not displayed here). Thorium contents remain relatively stable (as do Cu, Zn, Pb, and the REE, not displayed here) in granite-hosted SMI and are identical to those in pumice. Furthermore, the compositional trends are anchored on the "least evolved" (i.e. low-Cs) side of the granite-hosted inclusions (Figure 6d) to the composition of the more constant pumice-hosted inclusion assemblages (Figure 6d). Some elements such as Nb (and Be, Ta, not displayed here), are apparently characterized by a more abrupt increase in concentration in the granite-hosted inclusion assemblages.

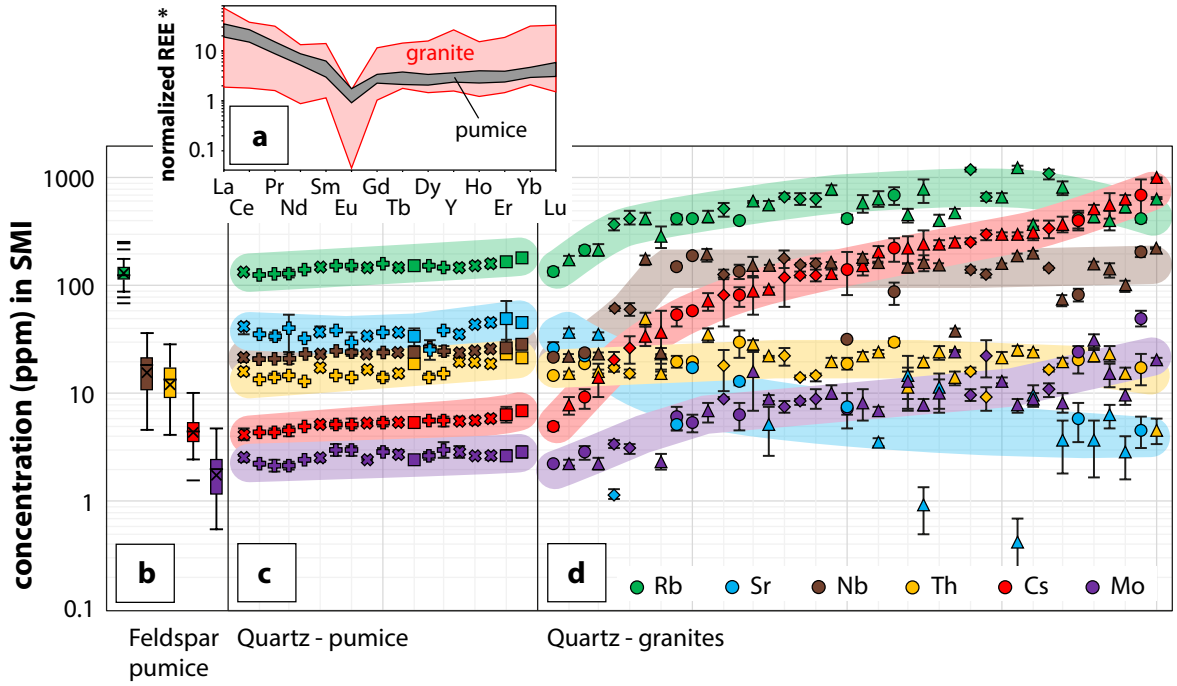

Figure 6: (a) Rare earth element (REE) diagram, * normalized to primitive mantle compositions from Sun and McDonough (1989). (b-d) Selected trace element concentrations in SMI assemblages hosted in: (b) plagioclase from pumice (box plot based on sample KPT04-21 from KPT unit E), (c) quartz from pumice, and (d) quartz from granite. In (b), the boxes correspond to ca. 50% of the analyses across several assemblages and the whiskers to the total range apart from a few outliers shown as dashes. Crosses and bars within the boxes represent the average and median, respectively. Several trails (primary and secondary) of four different plagioclase crystals were analyzed. In (d, e), each symbol represents an assemblage of several SMI with their 1σ standard deviation (see Methods for details). Different symbols represent different samples: square = KPT04-2 (pumice, unit B), cross = KPT04-5 (pumice, unit D), plus = KPT04-21 (pumice, unit E), circle = NIS-U39 (granite), triangle = NIS-Andi (granite), diamond = NIS37 (granite). The data are sorted by ascending Cs concentration to represent the evolution of the melt composition (Audétat and Pettke, 2003).

Some element concentrations are of particular interest for the formation of magmatic-hydrothermal ore deposits. These include ore metals, complexing ligands (e.g., Pokrovski et al., 2013), and fluxing elements (e.g., Bartels et al., 2011). Notably, concentrations of Cu and Mo determined by LA-ICP-MS in the pumice-hosted SMI are 1.9 ± 0.2 ppm and 2.7 ± 0.3 ppm, respectively. While Cu concentrations stay constant within uncertainty, Mo concentrations increase by an order of magnitude in the granite-hosted SMI. According to EPMA, concentrations

of Cl are in the range of 700-1000 ppm and 550-1300 ppm in pumice- and granite-derived SMI, respectively. Sulfur concentrations are below the detection limit of ca. 150 ppm in granite-derived SMI and below or close to the detection limit of ca. 120 ppm in pumice-derived SMI. Fluorine concentrations are below the detection limit of ca. 420 ppm in pumice-derived SMI but apparently above the detection limit in granite-hosted SMI. However, for unknown reasons, apparent concentrations of F are similar to those in the quartz host (around 1000-2000 ppm). The highest apparent F concentrations were encountered in SMI from sample NIS-U39 (around 2000-2800 ppm).

4.5 Fluid compositions as determined by LA-ICP-MS

The element-to-Na ratios are very similar in all inclusion types for K, Rb and Cs (Figure 7) – and probably Zn, Mo, and W although insufficient data was detected in the vapors for these elements. Considering the similar Na concentrations of the ID fluid and the vapor, their absolute element concentrations are also very similar. However, the ratios Mn/Na, Fe/Na, and Pb/Na are elevated in the vapor compared to the ID fluid. In the brine, Li/Na, B/Na, As/Na, and possibly Cu/Na are significantly depleted compared with the vapor and ID fluid inclusions. Many of the heavier elements such as Sr, Ba, La, Ce, Tl, Bi, and U could only be detected in the brine, where they are present in low amounts (ratios to Na mostly <0.001). In terms of estimated absolute concentration using Na as internal reference, most elements are most abundant in brine inclusions (salinity between ca. 35-50 wt% $NaCl_{equivalent}$), with the exception of B, As and potentially Li. To summarize (Table 3), the most abundant elements beside Cl carried by all three fluid types are Na, K, Fe, and Mn. Other components including Cu, Zn, Mo, and W are present in concentrations lower by order(s) of magnitude.

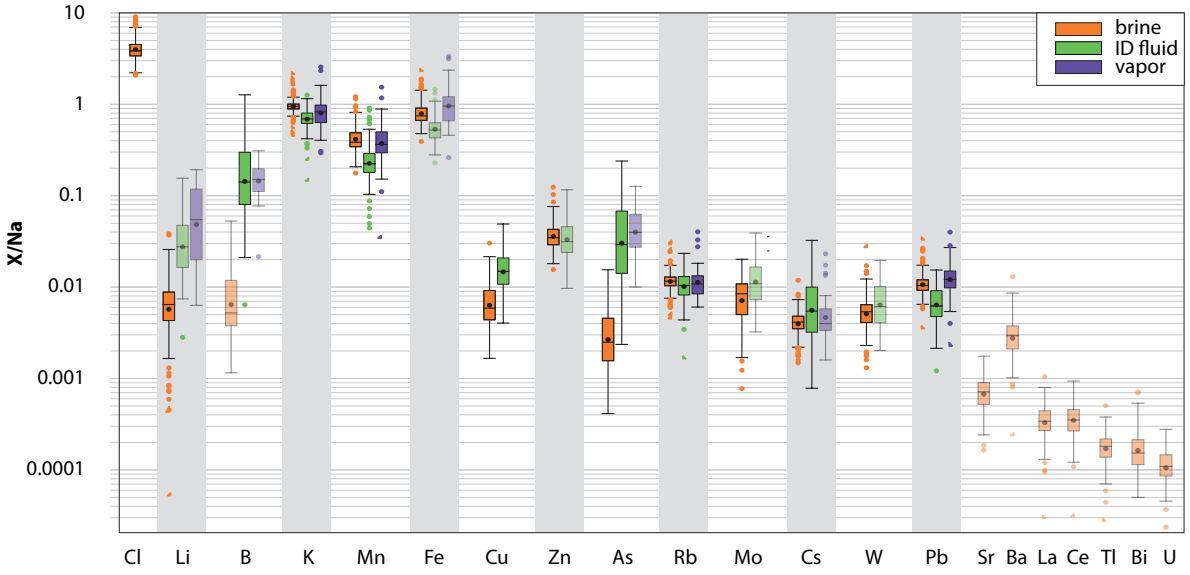

Figure 7: Box plot summarizing the compositions (expressed as element ratios to Na) of all fluid inclusions studied here, subdivided by fluid inclusion type (brine, ID fluid, and vapor). The boxes correspond to 50 % of the analyses across all analyzed assemblages, the whiskers correspond to 1.5 times the box length. Outliers are shown as separate, colored dots. Black dots and bars within the boxes represent the average and median, respectively. Elements detected in >50 % of the analyzed inclusions of the same fluid type are displayed with full color, while those between 25 and 50 % detection are displayed with lower opacity. Analyses separated by sample and assemblages can be found in the Appendix.

Table 3: Approximate concentrations ranges of selected elements in the different fluid types. Values in gray if often below detection limit. <D.L. = commonly below detection limit.

	Na (wt%)	K (wt%)	Fe (wt%)	Mn (wt%)	Cu (ppm)	Zn (ppm)	Mo (ppm)	W (ppm)	B (ppm)	As (ppm)
ID fluid	0.8-2.0	0.5-1.6	≤0.5-2	0.1-0.5	100-500	150-1000	50-300	50-200	350-8000*	40-1300*
Vapor	0.15-1.7	0.15-1.6	≤0.2-2	0.03-0.9	<D.L.	<D.L.	<D.L.	<D.L.	300-4000	300-1000
Brine	6.5-10.5	6-11	5-6.5	2-3.5	300-1000	2000-5000	100-1000	200-700	200-1700	100-650

* outlier at 14000 ppm B and 2200 ppm As

5 Discussion

5.1 Crystallization conditions of the magmatic host quartz

Several lines of evidence point to an origin of the granitic clasts from the rind of the KPT-forming magma reservoir (Bachmann, 2010). The largely overlapping Ti and Al concentrations (and Al/Ti ratios) in quartz from pumice and granitic clasts analyzed here (Figure 2a and c), as well as the compositional overlap of pumice-hosted and the least-evolved granite-hosted SMI (Figure 6c and d) further corroborate their co-magmatic origin. This means that pumice and granite crystallized from magmas of similar composition that resided in the same reservoir.

Concentric, oscillatory zoning, as commonly observed in both pumice and granite quartz, the resorption features of some crystals, and the presence of SMI demonstrate quartz crystallization from a magma under locally variable conditions (pressure, temperature, and/or composition) in the crystal mush. Based on the very similar range of Ti concentrations of the quartz in pumice and granitic clasts (mostly 50-80 ppm Ti), most of the quartz in both sample types crystallized at a temperature of predominantly ca. 760-700 °C (if $aTiO_2 = 0.6$ is assumed; higher $aTiO_2$ would yield lower temperatures; Huang and Audétat, 2012). This low temperature is in agreement with crystallization from a water-rich, rhyolitic melt and consistent with previously published magma storage temperatures at depth (700-780 °C, based on various geothermometers; Bachmann, 2010; Bachmann et al., 2007). Resorption features, CL bright zones with higher Ti concentrations, and the presence of SMI further indicate intermittently changing conditions, e.g., due to recharge with higher-temperature, potentially more mafic magma. Mafic recharge is also recorded by locally banded pumices (Allen, 2001).

While pumice quartz displays a very limited range in trace element (Al, Ti, Li) concentrations (Figure 2), granite quartz exhibits an overall larger range, extending to higher Al and lower Ti concentrations. Lower Ti concentrations indicate lower crystallization temperatures of the quartz (at constant $aTiO_2$), which is expected from higher crystallinity of the granites. The elevated Al concentrations compared to the bulk of the quartz, however, cannot be explained by simple cooling. Very high Al concentrations (>500 ppm) are commonly found in quartz crystallized from flux-enriched, pegmatitic melts (e.g., Breiter et al., 2012, and references therein). Here, high Al (and Li) concentrations might correspond to quartz crystallized from extremely fractionated melts. Possible explanations for the marked difference in Li concentrations between granite- and pumice-derived quartz may include fractionation of the interstitial melt (e.g., Lee and Morton, 2015) or syn-eruptive Li mobility (Ellis et al., 2018).

5.2 Relative timing of inclusion entrapment

Silicate melt inclusions are usually considered primary even if they do not outline crystal growth zones (Lowenstern, 1995). Indeed, crystallization of quartz and feldspars was clearly still ongoing in the KPT magma that gave rise to the juvenile pumices containing abundant SMI in phenocrysts. The position of many granite-hosted SMI, fluid and mixed fluid-SMI trails crossing quartz growth zoning in the crystal margin and in some cases extending to the crystal rim (the-

oretically classifying them as pseudo-secondary and secondary) places their entrapment after the crystallization of (most of) the quartz.

The abundance of fluid inclusion assemblages in the granitic clasts contrasts the paucity of preserved fluid in the pumice samples. However, the melt was likely fluid saturated already at an early stage, as suggested by the high initial water content of the magma (as indicated, e.g., by hornblende-bearing mafic enclaves; Voegelin et al., 2014). Furthermore, Voegelin et al. (2014) argued based on Mo concentrations that fluid saturation in the upper crustal magma reservoir occurred already at ca. 67 wt% SiO_2 of the KPT magma. Therefore, the lack of fluid inclusions in the pumice samples likely reflects unsuitable entrapment conditions, not an absence of exsolved fluids. In addition, the earliest exsolved fluids in such systems are expected to be more CO_2-rich (because of the low solubility of CO_2 in silicate melt in the upper crust), and their higher internal pressure is expected to lead to a lower preservation potential.

At intermediate crystallinity (ca. 40-70 vol% crystals), channelization of the fluids through the crystal mush enables efficient outgassing (i.e., upward migration of the fluid toward the roof; Lamy-Chappuis et al., 2020; Parmigiani et al., 2017). Only at high crystallinity (>70 vol% crystals; i.e., in a stiff granitic cap or wall of the magma chamber), where capillary fracturing dominates, and the mechanical interaction of touching crystals creates local stresses for the formation of microfractures, will bubbles likely be trapped (Degruyter et al., 2019; Parmigiani et al., 2017) in pseudo-secondary trails.

The highly variable trace element concentrations in granite-hosted SMI assemblages (Figure 6) result predominantly from fractional crystallization, as evidenced by the common increase of incompatible elements (except Th, which may be incorporated in significant amounts in accessory minerals such as monazite, zircon, and apatite; Figure 6c and d). In addition, a decrease in Sr (and Ba) and the deeper Eu anomaly in granite- compared to pumice-hosted SMI point to abundant crystallization of feldspar, and higher LREE/HREE ratios in pumice- compared to granite-hosted SMI assemblages (Figure 6b) indicate fractionation of monazite and/or apatite. Fluid fluxing could have played only a minor role for the SMI trends, as fluid immobile elements (exemplified by Ta) also increase from the pumice- to the granite-hosted SMI assemblages (Figure 6c and d), while fluid saturation of the melt is expected throughout the SMI record (Voegelin et al., 2014). Consequently, a range of crystallinities between 40 % to >99 % can be tentatively calculated using Cs concentrations in the melt (Audétat and Pettke, 2003) and assuming pure Rayleigh fractionation with a bulk partition coefficient between 0.025 and 0.5. Co-existing fluid inclusions were found over a range of crystallinities, but more frequently at elevated crystallinity. Therefore, the near-solidus assemblage should be well-represented by the wet haplogranite system and can be used to find the true entrapment conditions (Figure 4a; see also, e.g., Audétat and Pettke, 2003; Zajacz et al., 2008). It has to be noted, however, that at very high crystallinity, trace element concentratios are likely subject to the local crystallization environment and may not necessarily represent the bulk, interconnected melt. Boundary layer effects are unlikely to play a significant role because no correlation of element concentrations with inclusion size was observed.

5.3 Heterogeneous entrapment of silicate melt and fluid: pressure variations in the magma chamber

Direct exsolution of an ID fluid from the silicate melt (Figure 3e) and immiscibility of brine and vapor (Figure 3h) are expressed by heterogeneous entrapment (e.g., Goldstein and Reynolds, 1994) within the same assemblage and/or within the same inclusion cavities. The co-existence of brine and vapor requires the fluid system to be in the two-phase (vapor-liquid) field, while the ID fluid formed in the single-phase field. All fluid types can be encountered in the same

sample. Therefore, the diversity and co-existence of fluid inclusion types must record a change in the intensive variables of the system. Heterogeneous entrapment of silicate melt and brine (Figure 3f) and the high homogenization temperatures of the brine require this change to have occurred above the solidus (>650-670 °C).

Estimations of entrapment conditions (Figure 4) using the fluid system H_2O-NaCl (Driesner and Heinrich, 2007; Sourirajan and Kennedy, 1962) suggest that the samples experienced a large drop in pressure from around 170 to 100 MPa, to change from ID fluid saturation to vapor and brine entrapment, assuming that all inclusion types represent fluids that were exsolved from the same high-crystallinity magma as indicated by their common chemical characteristics. The application of the well-studied but simplified H_2O-NaCl system is reasonable because no large systematic offsets in pressure-temperature calculations are expected when neglecting KCl and because only very minor amounts of CO_2 are present in the brine and the ID fluid. However, some degree of uncertainty has to be expected in light of the chemical complexity of the fluid system (H_2O-CO_2-NaCl-KCl-...) compared to the simplified equations of state applicable.

The incipient KPT eruption would be a likely scenario to generate a large pressure drop, releasing chamber overpressure by fracturing the rock column above the magma chamber and by removing hundreds of meters of overburden. Estimates of the "critical" chamber overpressure required to cause a volcanic eruption by propagation of dikes from the chamber to the surface commonly range between 10 and 40 MPa (usually taken from Jellinek and DePaolo, 2003; e.g., Caricchi et al., 2014; Degruyter and Huber, 2014; Malfait et al., 2014; Tramontano et al., 2017; see also Karlstrom et al., 2009, and references therein; Rubin, 1995). Smaller pre-KPT eruptions (not removing significant overburden) now covered by the KPT and the concurrent release of fluid pressure may be invoked in the formation of vapor and brine, but do not explain the poor textural equilibration of many of the inclusions. Heating due to mafic recharge may have played a secondary role in transitioning from the single- to the two-phase field. Addition of CO_2 to the fluid (very little or no measurable CO_2 in the ID fluid vs. significant CO_2 in the vapor) may also be explained by mafic recharge close to the eruption, which does not only introduce more CO_2-rich fluids but may also enhance heating-related decarbonization of the wall rocks (e.g., Caricchi et al., 2018; Evans et al., 2016).

The detailed record of inclusion entrapment in a single microcrack shown in Figure 5 adds further constraints to this issue. We interpret this assemblage as evidence for rapid co-entrapment of brine with ca. 40 wt% $NaCl_{equivalent}$ and vapor, whereby the two phases compositionally separated further either due to the local pressure drop during microcrack formation or due to partial re-opening of an already existing, healed microcrack. This likely led to water transfer from the brine to the adjacent vapor (i.e., producing a brine with higher salinity; inset of Figure 5).

The unusual preservation of this dis-equilibrium state of a fluid inclusion assemblage and the unusually immature state of inclusion healing in this assemblage, despite high temperatures, indicates that not only the microcracking occured rapidly but also the available time duration for healing was very short (on the order of hours to days) by inference from experiments producing synthetic fluid inclusions (noting, however, that timescales of textural equilibration depend not only on temperature, but also on the width of the fluid-filled crack and the density and composition of the fluid; see, e.g., Bodnar, 2003; Bodnar et al., 1985; Pêcher and Boullier, 1984; Vanko et al., 1988; Vityk and Bodnar, 1995). Vapor inclusions with a very high salinity, a relatively large proportion of liquid, and some CO_2 that coexist with brine (Figure 3j) might represent an earlier fluid generation, which appears to be preserved only in a few assemblages. Other inclusions that may have been present were likely destroyed because the presence of CO_2 causes high internal pressurization to buid up upon decompression. This fluid is not included in the following discussion.

5.4 Element distribution between ID fluid and silicate melt, and between vapor and brine

The distribution of elements between co-existing phases (Figure 8) determines the ore-forming potential of the fluids. The first, primary magmatic fluid of the KPT is a single-phase ID fluid with relatively low salinity (ca. 3-11 wt% $NaCl_{equivalent}$), similar to the most primitive fluids reported also from the roots of numerous porphyry deposits (e.g., Klemm et al., 2008; Landtwing et al., 2010; Rusk et al., 2004; Stefanova et al., 2014). This fluid is capable of extracting Cu, Zn, Mo, Pb, W, As, and B from the silicate melt (by preferential partitioning into the ID fluid), whereas Rb and Cs show the opposite behavior (Figure 8a-b). The elements Li and Sb are commonly below the detection limit (especially in the ID fluid). A tendency toward stronger partitioning into the ID fluid with increasing fluid salinity is observed for many (reliably analyzable) elements such as Na, K, Mn, Rb, and Pb but not for B and As (Figure 8e and f).

Even higher concentrations for most elements were found in the brine (Figure 8c and d). However, element distribution between brine and vapor is more difficult to estimate because of low element concentrations in combination with the low density of the vapor; high detection limits therefore prohibit calculation of reliable partition coefficients between the two phases for many elements. The elements Rb, Cs, and Pb (well detected in both phases) prefer the brine over the vapor phase, while B and As (very limited data, commonly only returning detection limits) rather tend to accumulate in the vapor (Figure 8c and d). This disparity is broadly in agreement with experimentally determined partitioning (e.g., Pokrovski et al., 2008; Schatz et al., 2004). Considering that the salinities of the ID fluid and the vapor inclusions, which are maximum values given the potential accidental entrapment of co-existing brine (see below), are relatively low, the mass proportion of brine compared to vapor must have been small. For example, if we assume that an ID fluid of 10 wt% $NaCl_{equivalent}$ splits into a brine of 40 wt% $NaCl_{equivalent}$ and a vapor of 2 wt% $NaCl_{equivalent}$, the mass ratio of brine to vapor would be ca. 20:80. The proportion of brine drops below 10 % by mass (and even less by volume) if we assume that the ID fluid has only 5 wt% $NaCl_{equivalent}$.

Heterogeneous entrapment of a small amount of brine along with vapor inclusions can be a major obstruction in obtaining meaningful clues about the density or element concentrations of the pure vapor. Such inclusions are expected to show higher salinities (and lower clathrate melting temperatures). To exclude obvious cases from quantitative analysis, higher-salinity outliers within an assemblage were identified during microthermometry. Nevertheless, temperatures of clathrate melting in vapor inclusion assemblages are overall less consistent than temperatures of ice melting in ID inclusions, even in petrographically consistent assemblages, and some vapor inclusion assemblages exhibit a high salinity – in some cases even higher than that of ID

Figure 8 ***(following page)*:** Element distribution between (a, b) SMI and ID fluid inclusions and (c, d) brine and vapor inclusions. Each point represents one inclusion assemblage of two coexisting phases. Error bars represent 1σ uncertainty. The black diagonal lines separate the field of preferred partitioning into one or the other phase. The numbers on diagonal (black and grey) lines correspond to: (a, b) K_d = element concentration (by weight) of element i [ID fluid / silicate melt] and (c, d) K_d = element concentration of element i [vapor / brine]. In (a, b), two assemblages are distinguished with different symbols (square = NIS-Andi, 3.9 wt% $NaCl_{equivalent}$; triangle = NIS-Andi, 2.8 wt% $NaCl_{equivalent}$; note that most other assemblages of SMI and ID fluid inclusions are from the same sample) because they plot outside the range of the rest of the data for many elements. (e, f) Salinity from microthermometry vs. K_d(ID fluid / silicate melt) as in Figure 8a-b. Assemblages with less than 50% of the analyzed inclusions returning data above the detection limit for a specific element were plotted as symbols with low opacity.

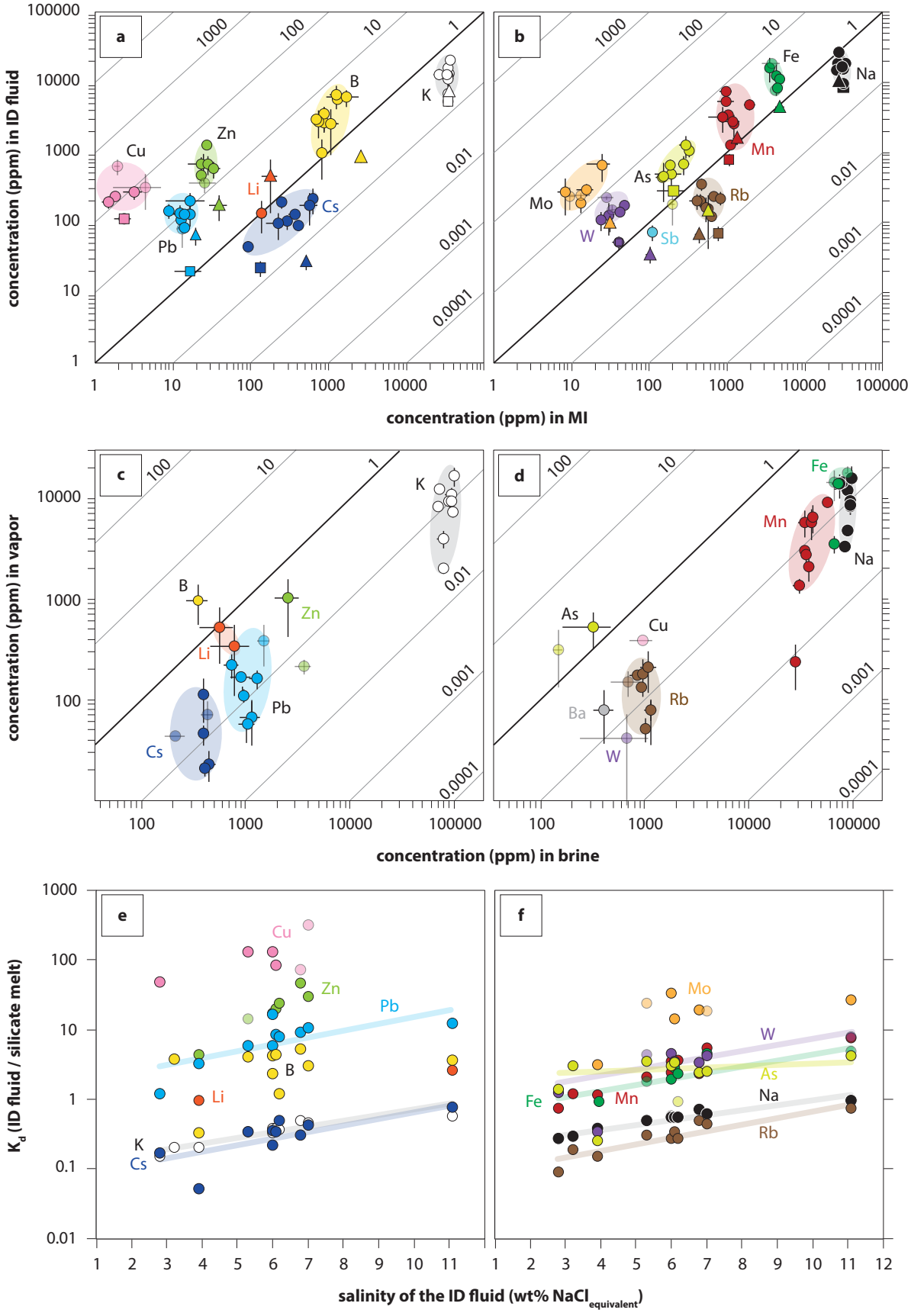
a
b
c
d
e
f
concentration (ppm) in ID fluid
concentration (ppm) in MI
concentration (ppm) in vapor
concentration (ppm) in brine
K_d (ID fluid / silicate melt)
salinity of the ID fluid (wt% $NaCl_{equivalent}$)
Cu
Zn
Pb
Li
B
Cs
K
Mo
W
As
Sb
Rb
Mn
Fe
Na
Ba

inclusions (Table 2). Furthermore, lower-salinity vapors are not consistently associated with higher-salinity brines, contrary to what would be expected based on the shape of the vapor-brine solvus (e.g., Driesner and Heinrich, 2007; see also Figure 5). Finally, Mn/Na, Fe/Na, and Pb/Na are similarly elevated both in the brine and the vapor compared to the ID fluid (Figure 7), although they are expected to be lower in the vapor phase due to strong partitioning into the brine. Collectively, this indicates heterogeneous entrapment of small but significant amounts of the wetting liquid (brine) phase, even in some apparently well-separated vapor inclusions. Consequently, element distribution between brine and vapor (Figure 8c and d) has to be regarded with reservation, as the true partitioning coefficients may be shifted to higher and lower values for vapor- and brine-oriented elements, respectively.

5.5 Comparison of fluid-melt element partitioning with previously published data

The most extensive quantitative element distribution data between melt and fluid have been presented by Zajacz et al. (2008) based on natural inclusion assemblages and by Iveson et al. (2019) using an experimental approach. Many other publications focus on specific elements (e.g., Audétat and Li, 2017; Candela and Holland, 1984; Iveson et al., 2017; Tattitch and Blundy, 2017; and many more). A compilation of partitioning studies can be found in Pokrovski et al. (2013). Generally, variations may be explained by different bulk compositions (including ligand availability; e.g., rift-related alkaline Mt. Malosa pegmatite and Ehrenfriedersdorf A-type granitic pegmatite in Zajacz et al., 2008), and different pressure, temperature and pH (e.g., Pokrovski et al., 2013). An influence of F on element partitioning (Zhang and Audétat, 2017) in the KPT fluids is unlikely because of the low F concentrations.

Table 4: Comparison of fluid/melt partition coefficients with the literature.

Element	This study	Zajacz et al. (2008)	Iveson et al. (2019)
Li	(1.0-2.6)*	2–35	0.05–0.7
B	0.3–5.2	2–15	–
Na	0.3-1.0	1.5–25	–
K	0.2–0.6	0.25–0.55	0.1–0.55
Mn	0.7-7.7	0.8–10	0.1–2.7
Fe	0.9-4.6	0.4–3.5	–
Cu	(50-130)*	15–3000	8–82
Zn	4-46	8–30	0.5–6.5
As	0.3-4.3	–	–
Rb	0.1–0.7	0.4–1	0.1–0.6
Mo	(3–33)*	2–25	0.1–1.2
Cs	0.05-0.8	0.4–6	–
W	0.3–4.5	1–15	0.04–1.6
Pb	1-17	6–30	0.02–3

* Only few data points, may not be representative.

Partition coefficients from the present study agree very well with those of Zajacz et al. (2008) for K, Mn, Fe, Zn, and Mo (Table 4). Partition coefficients for the elements Li, B, Cu, Cs, W, and Pb determined here overlap with the lower end of those from Zajacz et al. (2008), and only the partition coefficients for Na do not overlap. Agreement with Zajacz et al. (2008) would be even better for some elements (in particular, B, Cs, W, Pb) if the two "outlier" assemblages were omitted (Figure 8, squares and triangles).

In contrast, the partition coefficients from this study are mostly at the higher end of the experimentally-determined values of Iveson et al. (2019), and only those for K and Rb compare well. Experimental partitioning studies have some advantages in comparison to analyzing natural inclusions, including: (1) the relatively precisely known formation (equilibration) conditions and the possibility to vary these conditions independently to explore their effects on partitioning, and (2) the accessibility of analytes without the limitation of inclusion entrapment, whereas natural fluid inclusions are very rare, e.g., in magmatic phenocrysts. However, there are also many experimental challenges, as detailed in Iveson et al. (2019). Specifically, Mo, Pb, Zn, and W partition coefficients may be affected by quench reactions, diffusive disequilibrium during short experimental runs, and/or interaction with the experimental capsule material (e.g., Borchert et al., 2010; Iveson et al., 2019; Schmidt et al., 2020; Zhang et al., 2018). For example, partition coefficients for W between fluid and melt range between 0.46-29.9 based on new data from synthetic fluid inclusions (compared to 0.04-2.8 when quench fluids are analyzed; Schmidt et al., 2020). The behavior of Li is not well understood, and contradicting data about Li partitioning is published (Iveson et al., 2019, and references therein); our limited dataset cannot solve the debate.

5.6 Implications for ore formation

No economic mineralization has been reported from the study area, although an extensive hydrothermal system is associated with the KNYVS, expressed in gas emissions from Lakki plain of Nisyros volcano (e.g. Bini et al., 2019) and hydrothermal veinlets and alteration of pre-KPT lavas seen in igneous xenoliths. The volcanically active tectonic setting at an extending arc with slow subduction and thinned crust is in contrast to the setting of most major porphyry Cu deposits in regions of compressive arcs and thickened crust, which may favor the accumulation of non- to little-erupting magma reservoirs and eventual wholesale fluid expulsion without volcanic eruption (Rohrlach and Loucks, 2005; Sillitoe, 2010, and references therein). Despite these differences, the exceptional preservation of magmatic fluids in inclusions from Kos provides insights that are also relevant for ore-forming magmatic systems.

Many favorable factors must converge to form economic deposits, but a high metal content of the primary magmatic fluid obviously favors ore formation (Audétat, 2019). The ejected SMI and fluid inclusions studied here can be compared with inclusions from miarolitic cavities in apparently barren and mineralized intrusions (Figure 9). Both formed at high temperature and record the magmatic fluid before precipitation of any hydrothermal minerals. Distinctively, the KPT inclusions were quenched quickly by volcanic eruption and are apparently undisturbed by later hydrothermal overprint. When compared to literature data (Audétat, 2019), the KPT fluids with their high Mo and W concentrations resemble highly-fractionated rare-metal granites (Figure 9a-d) rather than porphyry Cu systems. Unlike typical Mo and W granites, however, the fraction of this highly fractionated (residual) melt was probably small in the KPT system at the time of the KPT eruption. Hence, the highly evolved magma could not release a large amount of metal- and sulfur-carrying fluid into the crust, which – together with efficient fluid focusing and mineral precipitation – would have been a prerequisite to form an ore deposit (e.g., Burnham and Ohmoto, 1980). Copper concentrations in SMI from the KPT (ca. 2 ppm; Figure 8a) overlap with data from other barren systems (Audétat and Pettke, 2003; Zajacz et al., 2008) and are relatively low compared to Cu-mineralized systems (e.g., Dilles, 1987 – Yerington, bulk rock; Halter et al., 2005 – Bajo de la Alumbrera, SMI in various host phases; Zhang and Audétat, 2017 – Bingham Canyon, SMI in rhyolite and various other rock types). However, SMI data from mineralized systems, in particular, may have suffered from post-entrapment modification of the Cu concentrations (Zajacz et al., 2009).

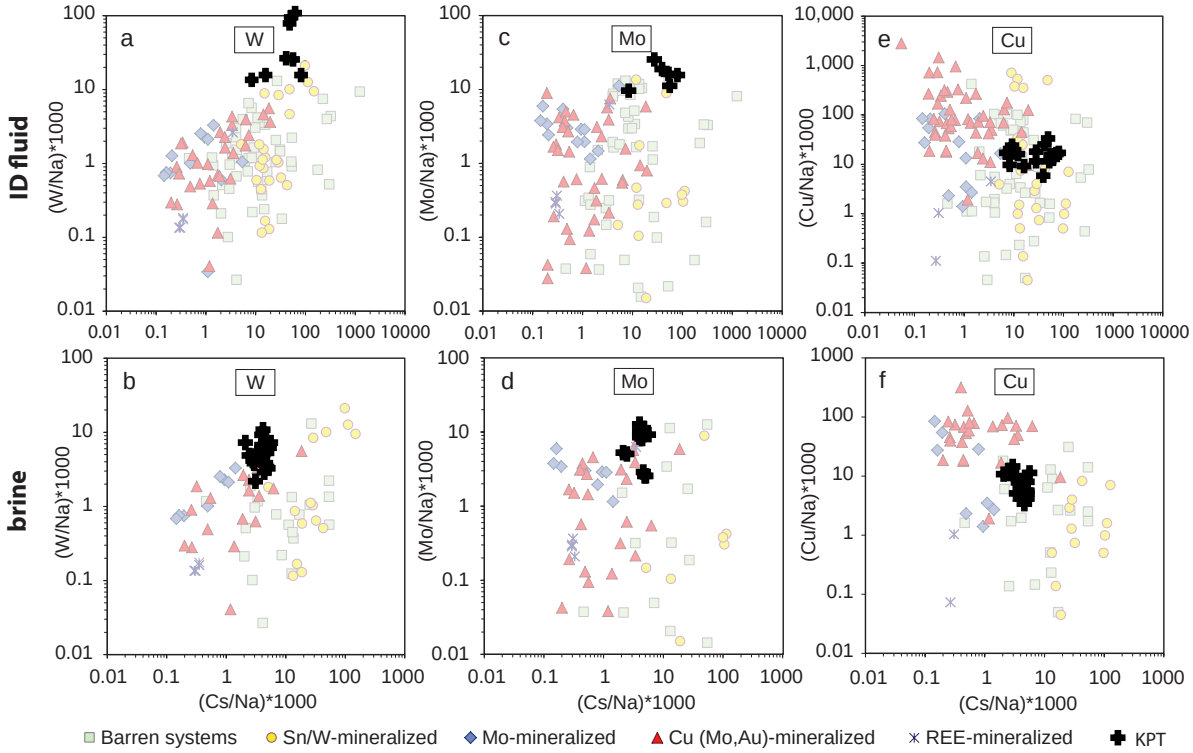

Figure 9: Comparison of metal concentrations in ID fluid and brine inclusions normalized to Na between KPT and other systems. The Cs/Na ratio serves as an indication of fluid differentiation. Modified from Audétat (2019).

Original Cu contents in low- to intermediate-salinity fluids generating porphyry Cu deposits are still strongly debated because of post-entrapment modification, particularly of S-rich ID fluid and vapor inclusions (Lerchbaumer and Audétat, 2012; Seo and Heinrich, 2013). If the extremely rapid formation and immediate quenching of inclusions due to the KPT eruption indeed prevented post-entrapment diffusional exchange, especially of the ID fluid and vapor inclusions, the measured Cu contents in primary magmatic fluids from the KPT represent some of the best estimates of original, unmodified metal concentrations in magmatic fluids exsolved in the upper crust. We stress, however, that the earliest exsolved fluids were probably not entrapped, as exsolution already started at low crystallinity. Moreover, a large pressure drop at nearly constant temperature would be unfavorable for the preservation of any ID fluid inclusions entrapped at higher pressure. This may also explain why samples with measurable fluid inclusions are generally rare in volcanic ejecta. Copper concentrations of the ID fluid of ca. 100-500 ppm (Figure 8a) are in good agreement with model predictions (Candela and Holland, 1984: 20-500 ppm; Chelle-Michou et al., 2017: 30-700 ppm Cu in fluid at ca. 770 °C) and mass balance calculations (Cline and Bodnar, 1991). Hence, thousands of ppm Cu as commonly seen in inclusions hosted bymagmatic-hydrothermal ore deposits may merely be the effect of diffusional re-equilibration (Lerchbaumer and Audétat, 2012; Seo and Heinrich, 2013) and not a necessary requirement for the formation of large ore deposits (e.g., Chelle-Michou et al., 2017).

6 Conclusions

The SMI and fluid inclusion associations of the KPT suggest a large and rapid change in pressure indicative of an incipient volcanic eruption – likely the KPT eruption. This eruption led to

quenching of the clasts and, thus, termination of the process of textural inclusion equilibration (healing). The proposed evolution is summarized in Figure 10. Initially, intermediate magmas were emplaced incrementally at around 200 MPa (see Bachmann and Huber, 2016; Cashman et al., 2017; Huber et al., 2019 for reviews on the assembly of large, upper crustal magma chambers), and a stratovolcano formed by lavas of variably evolved compositions ascending to the surface. As the reservoir grew, a rhyolitic cap progressively formed (Bachmann and Bergantz, 2004; Hildreth, 2004). During crystallization of the water-rich silicic magma in the upper crust, saturation of a single-phase (intermediate-density) fluid of relatively low salinity was reached. At this stage, part of the exsolved fluid migrated upward, where it caused hydrothermal alteration in previously erupted lavas and ultimately reached the surface, while some of the fluid got entrapped as inclusions in the high-crystallinity cap or wall zone (Figure 10a). Hot recharge from deeper in the system lead to re-heating of the crystal mush and thereby probably initiated eruption (Figure 10b; e.g., Bachmann et al., 2007). The eruption (and possibly the related magma ascent) caused a massive pressure drop, which transfered the exsolving fluid into the two-phase field and led to inclusion entrapment of immiscible brine and vapor (Figure 10c). Shortly after the initiation of the KPT eruption, the KPT eruption climax fragmented large parts of the granitic cap (and walls) and entrained them as co-genetic granitic clasts in KPT unit E (Figure 10d). The duration of the KPT eruption was in the range of hours to days (Allen, 2001), and the repose time between eruption stages was apparently just long enough for immature fluid inclusions to form.

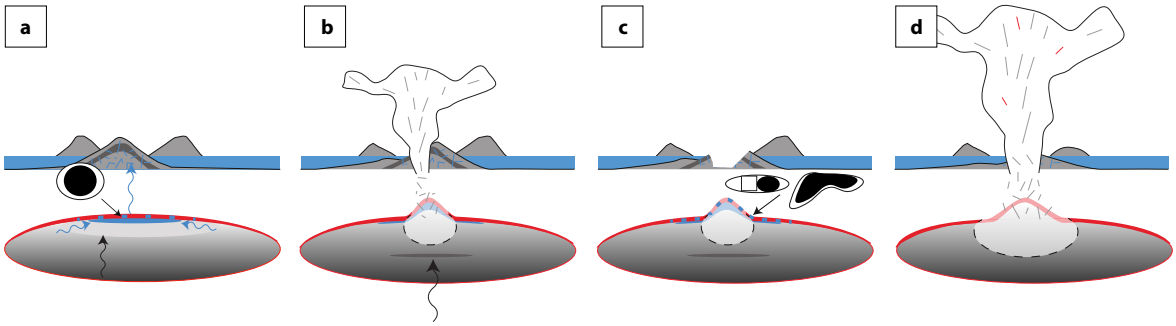

Figure 10: Sketch of fluid evolution in the magma chamber before and during the KPT eruption. (a) Differentiation of intermediate crystal mush, accumulation of rhyolitic melt in cap (light gray), fluid-saturation of silicic mush, formation of high-crystallinity granitic rind (red), fluid flow toward the roof of the chamber, entrapment of ID fluid in the granitic rind, release of fluids and alteration of overlaying lavas. (b) Initiation of the KPT eruption, initial rupture of the magma reservoir, fragmentation in the conduit, and pressure drop causing the exsolving fluid to become immiscible brine and vapor. (c) Short period of repose after initial fragmentation and entrapment of brine and vapor as inclusions in the granitic carapace, before climactic eruption phase with entrainment of granitic clasts (d).

1. Pumice and granitic clasts from the KPT are co-genetic, representing the rhyolitic cap of the large, upper crustal magma reservoir and its crystallized rind, respectively. Both likely formed in the presence of silicate melt and fluid; the fluid inclusions, however, are much better preserved in the granite clasts, indicating more favorable conditions for inclusion entrapment than in the pumices.

2. Fluid inclusions record both the single-phase fluid exsolved from the melt during late-stage fractionation (now represented by ID inclusions), and brine and vapor phases which formed upon phase separation of the latter upon decompression immediately prior to eruption of the KPT.

3. Silicate melt and fluid inclusions from the KPT therefore record a "snapshot" of late-stage melt fractionation, fluid exsolution, and phase separation and suffered very little, if any, post-entrapment modification. As such, they can be used to better constrain fluid/melt and liquid/vapor partitioning of metals during the magmatic-hydrothermal transition. In highly-evolved, calc-alkaline, water-rich systems in the upper crust, base metals (including Cu), Mo and W efficiently partition from the silicate melt into the ID fluid. Most elements except B, As, and potentially Li got further enriched in the brine upon boiling.

This study shows that erupted volcanic materials can, in favorable cases, preserve information about the fluid saturation and fluid evolution of upper-crustal magma reservoirs - based on clasts of co-magmatic holocrystalline plutonics or possibly even altered and veined materials from the roof of hidden magma chambers. Such samples may be more common than expected, but may have been commonly overlooked in volcanological studies. They may provide unique insight into the composition and physical state of deep magmatic fluids that differ substantially from expanded fumarolic gases. If fluid inclusions in such samples are preserved through the eruption process, they are less likely to be subjected to modification by chemical diffusion, which commonly alters slowly-cooled fluid inclusions in exposed miarolitic cavities and hydrothermal ore deposits.

Acknowledgements

This work was supported by grant SNF 200021_178928 to OB. J. Allaz is thanked for assistance with EPMA, A. Jallas for thin- and thick-section preparation, T. Pettke for helpful discussion, B. Ellis and K. Kyriakopoulos (University of Athens) for support during field work. Reviews by A. Audétat, L. Danyushevsky, and an anonymous reviewer and editorial handling by W. Sun are greatly appreciated.

Appendix A. Brief sample description and occurrence of fluid and silicate melt inclusions

Table A: Sampling locations of the studied pumica and granite samples.

Sample	Description	Latitude, Longitude
KPT04-2	Crystal-poorpumice,unitB	36.76743, 27.12045
KPT04-5	Pumice,unitD	36.76995, 27.11363
KPT04-6	Pumice,unitD/E	36.77635, 27.12357
KPT04-8	Granite,unitE	36.80875, 27.11755
KPT04-9	Bandedpumice,unitE	36.80637, 27.11658
KPT04-20	Granite,unitE	36.82880, 27.05107
KPT04-21	Pumice,unitE	36.82880, 27.05107
KPT04-24	Pumice,unitE	36.96318, 26.95490
KPT05-4	Granite,unitE	36.72300, 26.91907
NIS-Andi	Granite,unitE	36.80915, 27.11930
NIS37	Granite,unitE	36.80745, 27.11933
NIS38	Granite,unitE	36.80752, 27.11573
NIS-U39	Granite,unitE	36.80913, 27.11926

Granitic clasts contain both SMI and different types of fluid inclusions, while only SMI were observed in (quartz from) pumice samples (see Table A and Figure A).

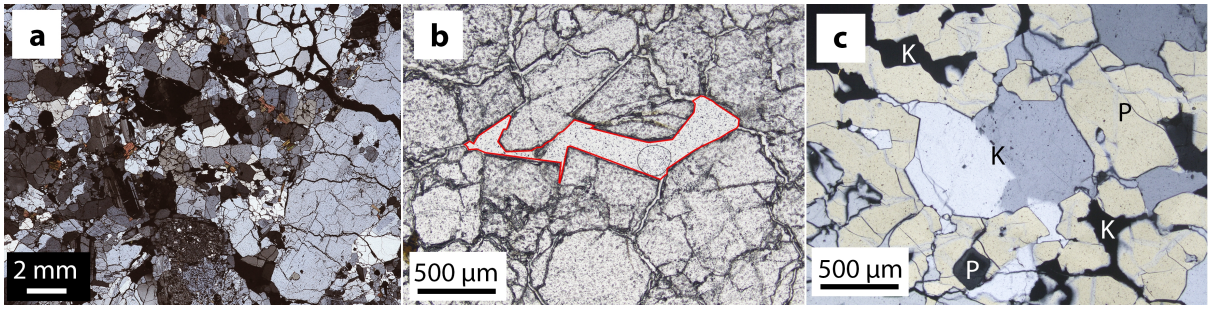

Figure A: Textures of co-genetic granitic clasts. (a) Coarse-grained sample NIS-Andi, showing some cracks. Composed of plagioclase (including one unusually large crystal), alkali feldspar, quartz, and biotite. (b) Micro-cavity (red line; now filled with epoxy) lined by euhedral crystal faces in sample NIS37. (c) Mineral intergrowth in coarse-grained sample NIS38. P = plagioclase, K = alkali feldspar. Plain view in (b), crossed Nichols in (a,c).

- Sample NIS-Andi contains abundant SMI assemblages and well-healed ID fluid inclusion assemblages. In some cases, assemblages of co-existing silicate melt and ID fluid were large and well-separated enough for analysis. Only few of these assemblages may be primary according to the shape of the trails. Brine and vapor assemblages appear to be absent, and no CO_2 could be detected in the ID fluid inclusions using Raman spectroscopy.

- Sample NIS-U39 contains abundant silicate melt, brine, vapor, and ID fluid inclusion assemblages. Assemblages of co-existing brine and vapor are common. Some assemblages of co-existing SMI and ID fluid inclusions were also observed, but there were often too few of the latter for analysis. Moreover, two assemblages of co-existing silicate melt and brine were observed, but could not be analyzed because the two phases were not sufficiently separated. Apparently there are also some assemblages with loosely associated high-density vapor and brine inclusions, at least some of which may be a result of local conditions around larger, now decrepitated inclusions.

- Sample NIS37 contains some SMI assemblages, vapor inclusion assemblages, and assemblages of co-existing silicate melt and ID fluid (usually too few ID fluid inclusions for analysis). Assemblages of brine and assemblages of co-existing vapor and brine are not very abundant. Sanidine crystals of this sample contain SMI assemblages, ID fluid inclusion assemblages, and mixtures of the two.

- Sample KPT04-20 contains abundant assemblages of ID fluid and of vapor and some SMI assemblages. Rare trails of relatively poorly-healed ID fluid inclusions were observed. No brine inclusion assemblages or assemblages of co-existing SMI and fluid inclusions were encountered.

Inclusions hosted by quartz were the focus of this study to unravel the compositions of fluids expelled by the KPT-forming magma because of its good inclusion preservation potential as a physically strong container without cleavage and its simple composition, facilitating data reduction. In addition, many feldspar crystals (especially plagioclase) were so crowded with inclusions that single assemblages could not be distinguished.

Silicate melt inclusions in quartz have well-rounded outlines or approximate negative crystal shape, while those in feldspars tend to be more elongate (compare Figures 3a and d). Necking and hourglass-shaped SMI can be found at crystal margins in pumice quartz (Figure 3b). The dominant type of SMI in quartz is glassy without or – less commonly – with a very small (<3 vol%) bubble and lacks any crystals (be it a daughter or accidentally entrapped phase).

Less common are SMI with emulsion textures, i.e. many bubbles of different sizes within the glass, and devitrified (finely crystallized), brown SMI. In a few cases, a small opaque crystal (usually attached to the bubble) or a hexagonal mineral flake is present. Very large (>200 μm) SMI are more likely to be decrepitated, as indicated by cracks crossing the inclusion or large bubble(s) (see also Bachmann et al., 2010b). In quartz of one sample (KPT05-4), many large SMI appear to have decrepitated and are now dark and irregularly-shaped (Figure 3c). Silicate melt inclusions in feldspars more typically contain one or several bubbles (Figure 3d). Assemblages of partially crystallized SMI, as indicated by deformed bubbles, were also observed but not analyzed.

Appendix B. Detailed view on element ratios for all studies fluid types

Figure B breaks down Figure 7 into separate samples and inclusion assemblages. Most element ratios are very consistent (within uncertainty) for the different fluid types across all samples and assemblages, with the exception of overall potentially lower Fe (commonly below detection limit) concentrations in the ID fluid in sample KPT04-20 and higher Fe/K ratios in the brine in sample NIS37. In addition, clear trends of element ratios with increasing salinity (for any fluid type) appear to be absent.

Most elements could be detected in the dense, saline brine inclusions, whereas the ID fluid and low-density vapor inclusions returned much fewer elements in concentrations above the detection limit, resulting in larger uncertainties and complicating the comparison between the different phases.

Intermediate-density fluid inclusion assemblages co-existing with silicate melt and vapor inclusions coexisting with brine (and vice versa) are distributed throughout the range of salinities. There is no systematic difference between assemblages with and without co-existing other phase. The two highest-salinity inclusion assemblages included in the ID fluid inclusion assemblages in Figure B (11.6 and 15.8 wt% $NaCl_{equivalent}$) correspond to rare assemblages of vapor with a large proportion of liquid ("VL" in Figure 3j) and apparently coexisting brine.

Supplementary material

Supplementary data to this article can be found online at https://doi.org/10.1016/j.gca.2020.03.038.

Figure B *(following page)*: Compositions of (a) ID fluid, (b) vapor, and (c) brine inclusion assemblages, expressed as ratios to Na to avoid introduction of additional uncertainty from the estimate of $NaCl_{equivalent}$. Each vertical bar (white/gray) represents one assemblage; different element ratios are spaced out within these bars to make the plot easier to read. Symbols represent the average of the assemblage; Bars represent 1-sigma uncertainty. Inclusion assemblages are sorted by sample and average salinity (wt% $NaCl_{equivalent}$, indicated above the plots). Only inclusion assemblages with at least 50% of the analyzed inclusions returning values above the detection limit for any one element are plotted in full opacity.

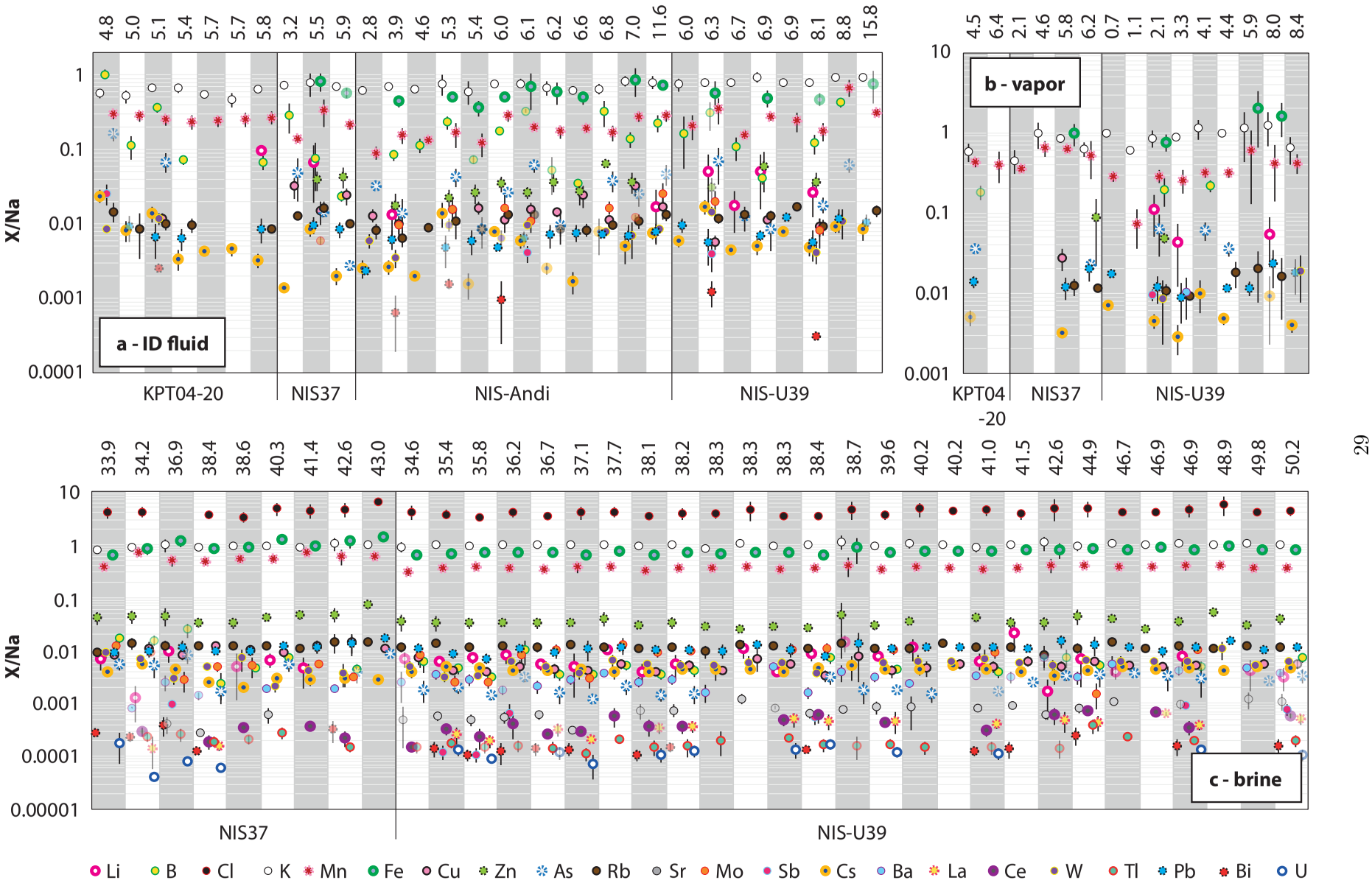
a - ID fluid
b - vapor
c - brine
X/Na
KPT04-20
NIS37
NIS-Andi
NIS-U39
KPT04 -20
Li B Cl K Mn Fe Cu Zn As Rb Sr Mo Sb Cs Ba La Ce W Tl Pb Bi U

References

Aiuppa, A., Baker, D. R., and Webster, J. D. (2009). Halogens in volcanic systems. *Chemical Geology*, 263(1-4):1–18.

Allen, S. R. (2001). Reconstruction of a major caldera-forming eruption from pyroclastic deposit characteristics: Kos Plateau Tuff, eastern Aegean Sea. *Journal of Volcanology and Geothermal Research*, 105(1-2):141–162.

Allen, S. R. and Cas, R. A. (1998). Rhyolitic fallout and pyroclastic density current deposits from a phreatoplinian eruption in the eastern Aegean Sea, Greece. *Journal of Volcanology and Geothermal Research*, 86(1-4):219–251.

Allen, S. R., Stadlbauer, E., and Keller, J. (1999). Stratigraphy of the Kos Plateau Tuff: Product of a major Quaternary explosive rhyolitic eruption in the eastern Aegean, Greece. *International Journal of Earth Sciences*, 88(1):132–156.

Audétat, A. (2019). The metal content of magmatic-hydrothermal fluids and its relationship to mineralization potential. *Economic Geology*, 114(6):1033–1056.

Audétat, A., Garbe-Schönberg, D., Kronz, A., Pettke, T., Rusk, B., Donovan, J. J., and Lowers, H. A. (2015). Characterisation of a natural quartz crystal as a reference material for micro-analytical determination of Ti, Al, Li, Fe, Mn, Ga and Ge. *Geostandards and Geoanalytical Research*, 39(2):171–184.

Audétat, A. and Li, W. (2017). The genesis of Climax-type porphyry Mo deposits: Insights from fluid inclusions and melt inclusions. *Ore Geology Reviews*, 88:436–460.

Audétat, A. and Pettke, T. (2003). The magmatic-hydrothermal evolution of two barren granites: A melt and fluid inclusion study of the Rito del Medio and Canada Pinabete plutons in northern New Mexico (USA). *Geochimica et Cosmochimica Acta*, 67(1):97–121.

Audétat, A., Pettke, T., Heinrich, C. A., and Bodnar, R. J. (2008). Special paper: The composition of magmatic-hydrothermal fluids in barren and mineralized intrusions. *Economic Geology*, 103(5):877–908.

Bachmann, O. (2010). The petrologic evolution and pre-eruptive conditions of the rhyolitic Kos Plateau Tuff (Aegean arc). *Open Geosciences*, 2(3):270–305.

Bachmann, O., Allen, S. R., and Bouvet de Maisonneuve, C. (2019). The Kos–Nisyros–Yali Volcanic Field. *Elements*, 15(3):191–196.

Bachmann, O. and Bergantz, G. W. (2004). On the Origin of Crystal-poor Rhyolites: Extracted from Batholithic Crystal Mushes. *Journal of Petrology*, 45(8):1565–1582.

Bachmann, O., Charlier, B. L. A., and Lowenstern, J. B. (2007). Zircon crystallization and recycling in the magma chamber of the rhyolitic Kos Plateau Tuff (Aegean arc). *Geology*, 35(1):73–76.

Bachmann, O., Deering, C. D., Ruprecht, J. S., Huber, C., Skopelitis, A., and Schnyder, C. (2012). Evolution of silicic magmas in the Kos-Nisyros volcanic center, Greece: A petrological cycle associated with caldera collapse. *Contributions to Mineralogy and Petrology*, 163(1):151–166.

Bachmann, O., Dungan, M. A., and Lipman, P. W. (2002). The Fish Canyon magma body, San Juan volcanic field, Colorado: Rejuvenation and eruption of an upper-crustal batholith. *Journal of Petrology*, 43(8):1469–1503.

Bachmann, O. and Huber, C. (2016). Silicic magma reservoirs in the Earth's crust. *American Mineralogist*, 101(11):2377–2404.

Bachmann, O., Schoene, B., Schnyder, C., and Spikings, R. (2010a). The 40Ar/39Ar and U/Pb dating of young rhyolites in the Kos-Nisyros volcanic complex, Eastern Aegean Arc, Greece: Age discordance due to excess 40Ar in biotite. *Geochemistry, Geophysics, Geosystems*, 11(8).

Bachmann, O., Wallace, P. J., and Bourquin, J. (2010b). The melt inclusion record from the rhyolitic Kos Plateau Tuff (Aegean Arc). *Contributions to Mineralogy and Petrology*, 159(2):187–202.

Bacon, C. R. and Lowenstern, J. B. (2005). Late Pleistocene granodiorite source for recycled zircon and phenocrysts in rhyodacite lava at Crater Lake, Oregon. *Earth and Planetary Science Letters*, 233(3-4):277–293.

Bakker, R. J. (2003). Package FLUIDS 1. Computer programs for analysis of fluid inclusion data and for modelling bulk fluid properties. *Chemical Geology*, 194(1):3–23.

Bakker, R. J. and Jansen, J. B. H. (1990). Preferential water leakage from fluid inclusions by means of mobile dislocations. *Nature*, 345(6270):58.

Bartels, A., Vetere, F., Holtz, F., Behrens, H., and Linnen, R. L. (2011). Viscosity of flux-rich pegmatitic melts. *Contributions to Mineralogy and Petrology*, 162(1):51–60.

Bini, G., Chiodini, G., Cardellini, C., Vougioukalakis, G. E., and Bachmann, O. (2019). Diffuse emission of CO2 and convective heat release at Nisyros caldera (Greece). *Journal of Volcanology and Geothermal Research*, 376:44–53.

Bodnar, R. J. (2003). Reequilibration of fluid inclusions. In Samson, I., Anderson, A., and Marshall, D., editors, *Fluid Inclusions: Analysis and Interpretation*, volume 32 of *Short Course*, pages 213–230.

Bodnar, R. J., Burnham, C. W., and Sterner, S. M. (1985). Synthetic fluid inclusions in natural quartz. III. Determination of phase equilibrium properties in the system H2O-NaCl to 1000 C and 1500 bars. *Geochimica et Cosmochimica Acta*, 49(9):1861–1873.

Borchert, M., Wilke, M., Schmidt, C., and Rickers, K. (2010). Rb and Sr partitioning between haplogranitic melts and aqueous solutions. *Geochimica et Cosmochimica Acta*, 74(3):1057–1076.

Bouvet De Maisonneuve, C., Bachmann, O., and Burgisser, A. (2009). Characterization of juvenile pyroclasts from the Kos Plateau Tuff (Aegean Arc): Insights into the eruptive dynamics of a large rhyolitic eruption. *Bulletin of Volcanology*, 71(6):643–658.

Breiter, K., Svojtka, M., Ackerman, L., and Švecová, K. (2012). Trace element composition of quartz from the Variscan Altenberg–Teplice caldera (Krušné hory/Erzgebirge Mts, Czech Republic/Germany): Insights into the volcano-plutonic complex evolution. *Chemical Geology*, 326-327:36–50.

Brombach, T., Caliro, S., Chiodini, G., Fiebig, J., Hunziker, J. C., and Raco, B. (2003). Geochemical evidence for mixing of magmatic fluids with seawater, Nisyros hydrothermal system, Greece. *Bulletin of Volcanology*, 65(7):505–516.

Brombach, T., Hunziker, J. C., Chiodini, G., Cardellini, C., and Marini, L. (2001). Soil diffuse degassing and thermal energy fluxes from the southern Lakki plain, Nisyros (Greece). *Geophysical Research Letters*, 28(1):69–72.

Brown, S. J. A., Burt, R. M., Cole, J. W., Krippner, S. J. P., Price, R. C., and Cartwright, I. (1998). Plutonic lithics in ignimbrites of Taupo Volcanic Zone, New Zealand; sources and conditions of crystallisation. *Chemical Geology*, 148(1):21–41.

Burnham, C. W. and Ohmoto, H. (1980). Late stage processes of felsic magmatism. In Ishihara, S. and Takenouchi, S., editors, *Granitic Magmatism and Related Mineralization*, number 8 in Mining Geology Special Issue. The Society of Mining Geologists of Japan, Tokyo.

Burt, R. M., Brown, S. J. A., Cole, J. W., Shelley, D., and Waight, T. E. (1998). Glass-bearing plutonic fragments from ignimbrites of the Okataina caldera complex, Taupo Volcanic Zone, New Zealand: Remnants of a partially molten intrusion associated with preceding eruptions. *Journal of Volcanology and Geothermal Research*, 84(3):209–237.

Caliro, S., Chiodini, G., Galluzzo, D., Granieri, D., La Rocca, M., Saccorotti, G., and Ventura, G. (2005). Recent activity of Nisyros volcano (Greece) inferred from structural, geochemical and seismological data. *Bulletin of Volcanology*, 67(4):358–369.

Candela, P. A. and Holland, H. D. (1984). The partitioning of copper and molybdenum between silicate melts and aqueous fluids. *Geochimica et Cosmochimica Acta*, 48(2):373–380.

Caricchi, L., Annen, C., Blundy, J., Simpson, G., and Pinel, V. (2014). Frequency and magnitude of volcanic eruptions controlled by magma injection and buoyancy. *Nature Geoscience*, 7(2):126–130.

Caricchi, L., Sheldrake, T. E., and Blundy, J. (2018). Modulation of magmatic processes by CO2 flushing. *Earth and Planetary Science Letters*, 491:160–171.

Cashman, K. V. and Scheu, B. (2015). Magmatic Fragmentation. In Sigurdsson, H., editor, *The Encyclopedia of Volcanoes (Second Edition)*, pages 459–471. Academic Press, Amsterdam.

Cashman, K. V., Sparks, R. S. J., and Blundy, J. D. (2017). Vertically extensive and unstable magmatic systems: A unified view of igneous processes. *Science*, 355(6331):1280–1288.

Charlier, B. L. A., Peate, D. W., Wilson, C. J. N., Lowenstern, J. B., Storey, M., and Brown, S. J. A. (2003). Crystallisation ages in coeval silicic magma bodies: 238U–230Th disequilibrium evidence from the Rotoiti and Earthquake Flat eruption deposits, Taupo Volcanic Zone, New Zealand. *Earth and Planetary Science Letters*, 206(3):441–457.

Chelle-Michou, C., Rottier, B., Caricchi, L., and Simpson, G. (2017). Tempo of magma degassing and the genesis of porphyry copper deposits. *Scientific Reports*, 7:40566.

Chiodini, G., Brombach, T., Caliro, S., Cardellini, C., Marini, L., and Dietrich, V. (2002). Geochemical indicators of possible ongoing volcanic unrest at Nisyros Island (Greece). *Geophysical Research Letters*, 29(16):1759–1732.

Chiodini, G., Cioni, R., and Marini, L. (1993). Reactions governing the chemistry of crater fumaroles from Vulcano Island, Italy, and implications for volcanic surveillance. *Applied Geochemistry*, 8(4):357–371.

Cline, J. S. and Bodnar, R. J. (1991). Can economic porphyry copper mineralization be generated by a typical calc-alkaline melt? *Journal of Geophysical Research: Solid Earth*, 96(B5):8113–8126.

De Vivo, B., Torok, K., Ayuso, R. A., Lima, A., and Lirer, L. (1995). Fluid inclusion evidence for magmatic silicate/saline/CO2 immiscibility and geochemistry of alkaline xenoliths from Ventotene Island, Italy. *Geochimica et Cosmochimica Acta*, 59(14):2941–2953.

Degruyter, W. and Huber, C. (2014). A model for eruption frequency of upper crustal silicic magma chambers. *Earth and Planetary Science Letters*, 403:117–130.

Degruyter, W., Huber, C., Bachmann, O., Cooper, K. M., and Kent, A. J. R. (2017). Influence of Exsolved Volatiles on Reheating Silicic Magmas by Recharge and Consequences for Eruptive Style at Volcán Quizapu (Chile). *Geochemistry, Geophysics, Geosystems*, 18(11):4123–4135.

Degruyter, W., Parmigiani, A., Huber, C., and Bachmann, O. (2019). How do volatiles escape their shallow magmatic hearth? *Philosophical Transactions of the Royal Society A: Mathematical, Physical and Engineering Sciences*, 377(2139):20180017.

DeMets, C., Gordon, R. G., Argus, D. F., and Stein, S. (1990). Current plate motions. *Geophysical journal international*, 101(2):425–478.

Diamond, L. W. (1992). Stability of CO2 clathrate hydrate + CO2 liquid + CO2 vapour + aqueous KCl-NaCl solutions: Experimental determination and application to salinity estimates of fluid inclusions. *Geochimica et Cosmochimica Acta*, 56(1):273–280.

Dilles, J. H. (1987). Petrology of the Yerington Batholith, Nevada; evidence for evolution of porphyry copper ore fluids. *Economic Geology*, 82(7):1750–1789.

Donovan, J. J., Singer, J. W., and Armstrong, J. T. (2016). A new EPMA method for fast trace element analysis in simple matrices. *American Mineralogist*, 101(8):1839–1853.

Donovan, J. J. and Tingle, T. N. (1996). An improved mean atomic number background correction for quantitative microanalysis. *Microscopy and Microanalysis*, 2(1):1–7.

Driesner, T. (2007). The system H2O–NaCl. Part II: Correlations for molar volume, enthalpy, and isobaric heat capacity from 0 to 1000°C, 1 to 5000bar, and 0 to 1 XNaCl. *Geochimica et Cosmochimica Acta*, 71(20):4902–4919.

Driesner, T. and Heinrich, C. A. (2007). The system H2O–NaCl. Part I: Correlation formulae for phase relations in temperature–pressure–composition space from 0 to 1000°C, 0 to 5000bar, and 0 to 1 XNaCl. *Geochimica et Cosmochimica Acta*, 71(20):4880–4901.

Dufek, J. and Bergantz, G. W. (2007). Dynamics and deposits generated by the Kos Plateau Tuff eruption: Controls of basal particle loss on pyroclastic flow transport. *Geochemistry, Geophysics, Geosystems*, 8(12).

Edmonds, M. (2008). New geochemical insights into volcanic degassing. *Philosophical Transactions of the Royal Society A: Mathematical, Physical and Engineering Sciences*, 366(1885):4559–4579.

Ellis, B. S., Szymanowski, D., Magna, T., Neukampf, J., Dohmen, R., Bachmann, O., Ulmer, P., and Guillong, M. (2018). Post-eruptive mobility of lithium in volcanic rocks. *Nature Communications*, 9.

Evans, B. W., Hildreth, W., Bachmann, O., and Scaillet, B. (2016). In defense of magnetite-ilmenite thermometry in the Bishop Tuff and its implication for gradients in silicic magma reservoirs. *American Mineralogist*, 101(2):469–482.

Fischer, T. P. and Chiodini, G. (2015). Volcanic, magmatic and hydrothermal gases. In *The Encyclopedia of Volcanoes*, pages 779–797. Elsevier.

Francalanci, L., Vougioukalakis, G. E., Perini, G., and Manetti, P. (2005). A West-East Traverse along the magmatism of the south Aegean volcanic arc in the light of volcanological, chemical and isotope data. In *Developments in Volcanology*, volume 7, pages 65–111. Elsevier.

Francalanci, L. and Zellmer, G. F. (2019). Magma genesis at the South Aegean Volcanic Arc. *Elements*, 15(3):165–170.

Fulignati, P., Kamenetsky, V. S., Marianelli, P., Sbrana, A., and Mernagh, T. P. (2001). Melt inclusion record of immiscibility between silicate, hydrosaline, and carbonate melts: Applications to skarn genesis at Mount Vesuvius. *Geology*, 29(11):1043–1046.

Goldstein, R. H. and Reynolds, T. J. (1994). *Systematics of Fluid Inclusions in Diagenetic Minerals*, volume no. 31 of *SEPM Short Course*. SEPM, Tulsa, Oklahoma.

Guillong, M., Hametner, K., Reusser, E., Wilson, S. A., and Günther, D. (2007). Preliminary characterisation of new glass reference materials (GSA-1G, GSC-1G, GSD-1G and GSE-1G) by laser ablation-inductively coupled plasma-mass spectrometry using 193 nm, 213 nm and 266 nm wavelengths. *Geostandards and Geoanalytical Research*, 29(3):315–331.

Guillong, M., Meier, D. L., Allan, M. M., Heinrich, C. A., and Yardley, B. W. (2008). Appendix A6: SILLS: A MATLAB-based program for the reduction of laser ablation ICP-MS data of homogeneous materials and inclusions. *Mineralogical Association of Canada Short Course*, 40:328–333.

Guillong, M., von Quadt, A., Sakata, S., Peytcheva, I., and Bachmann, O. (2014). LA-ICP-MS Pb–U dating of young zircons from the Kos–Nisyros volcanic centre, SE Aegean arc. *Journal of Analytical Atomic Spectrometry*, 29(6):963–970.

Günther, D., Frischknecht, R., Heinrich, C. A., and Kahlert, H.-J. (1997). Capabilities of an argon fluoride 193 nm excimer laser for laser ablation inductively coupled plasma mass spectometry microanalysis of geological materials. *Journal of Analytical Atomic Spectrometry*, 12(9):939–944.

Hall, D. L. and Sterner, S. M. (1995). Experimental diffusion of hydrogen into synthetic fluid inclusions in quartz. *Journal of Metamorphic Geology*, 13(3):345–355.

Halter, W. E., Heinrich, C. A., and Pettke, T. (2005). Magma evolution and the formation of porphyry Cu–Au ore fluids: Evidence from silicate and sulfide melt inclusions. *Mineralium Deposita*, 39(8):845–863.

Heinrich, C. A., Pettke, T., Halter, W. E., Aigner-Torres, M., Audétat, A., Günther, D., Hattendorf, B., Bleiner, D., Guillong, M., and Horn, I. (2003). Quantitative multi-element analysis of minerals, fluid and melt inclusions by laser-ablation inductively-coupled-plasma mass-spectrometry. *Geochimica et Cosmochimica Acta*, 67(18):3473–3497.

Helsel, D. R. (2012). *Statistics for Censored Environmental Data Using Minitab and R*. John Wiley & Sons, Inc., Hoboken, New Jersey, first edition.

Henley, R. W. and Seward, T. M. (2018). Gas–solid reactions in arc volcanoes: Ancient and modern. *Reviews in Mineralogy and Geochemistry*, 84(1):309–349.

Hildreth, W. (2004). Volcanological perspectives on Long Valley, Mammoth Mountain, and Mono Craters: Several contiguous but discrete systems. *Journal of Volcanology and Geothermal Research*, 136(3):169–198.

Holloway, J. R. (1981). Volatile interactions in magmas. In Newton, R. C., Navrotsky, A., and Wood, B. J., editors, *Thermodynamics of Minerals and Melts*, Advances in Physical Geochemistry, pages 273–293. Springer, New York, NY.

Huang, R. and Audétat, A. (2012). The titanium-in-quartz (TitaniQ) thermobarometer: A critical examination and re-calibration. *Geochimica et Cosmochimica Acta*, 84:75–89.

Huber, C., Townsend, M., Degruyter, W., and Bachmann, O. (2019). Optimal depth of subvolcanic magma chamber growth controlled by volatiles and crust rheology. *Nature Geoscience*, 12:762–768.

Humphreys, M. C., Kearns, S. L., and Blundy, J. D. (2006). SIMS investigation of electron-beam damage to hydrous, rhyolitic glasses: Implications for melt inclusion analysis. *American Mineralogist*, 91(4):667–679.

Innocenti, F., Manetti, P., Peccerillo, A., and Poli, G. (1981). South Aegean volcanic arc: Geochemical variations and geotectonic implications. *Bulletin Volcanologique*, 44(3):377–391.

Italiana, G. (1983). Nisyros 1 geothermal well: Final report: Petrographical logging, drilling, testing, sampling and new geochemical surface data, 6 June-3 December 1982. Technical report, Bruxelles: Luxembourg.

Iveson, A. A., Webster, J. D., Rowe, M. C., and Neill, O. K. (2017). Major element and halogen (F, Cl) mineral–melt–fluid partitioning in hydrous rhyodacitic melts at shallow crustal conditions. *Journal of Petrology*, 58(12):2465–2492.

Iveson, A. A., Webster, J. D., Rowe, M. C., and Neill, O. K. (2019). Fluid-melt trace-element partitioning behaviour between evolved melts and aqueous fluids: Experimental constraints on the magmatic-hydrothermal transport of metals. *Chemical Geology*, 516:18–41.

Jellinek, A. M. and DePaolo, D. J. (2003). A model for the origin of large silicic magma chambers: Precursors of caldera-forming eruptions. *Bulletin of Volcanology*, 65(5):363–381.

Jochum, K. P., Weis, U., Stoll, B., Kuzmin, D., Yang, Q., Raczek, I., Jacob, D. E., Stracke, A., Birbaum, K., and Frick, D. A. (2011). Determination of reference values for NIST SRM 610–617 glasses following ISO guidelines. *Geostandards and Geoanalytical Research*, 35(4):397–429.

Johannes, W. and Holtz, F. (1996). *Petrogenesis and experimental petrology of granitic rocks*, volume 22 of *Minerals and rocks*. Springer, Berlin, New York.

Kamenetsky, V. S. and Danyushevsky, L. V. (2005). Metals in quartz-hosted melt inclusions: Natural facts and experimental artifacts. *American Mineralogist*, 90(10):1674–1678.

Karlstrom, L., Dufek, J., and Manga, M. (2009). Organization of volcanic plumbing through magmatic lensing by magma chambers and volcanic loads. *Journal of Geophysical Research: Solid Earth*, 114(B10).

Keller, J. (1969). Origin of rhyolites by anatectic melting of granitic crustal rocks. *Bulletin Volcanologique*, 33(3):942–959.

Klaver, M., Matveev, S., Berndt, J., Lissenberg, C. J., and Vroon, P. Z. (2017). A mineral and cumulate perspective to magma differentiation at Nisyros volcano, Aegean arc. *Contributions to Mineralogy and Petrology*, 172(11-12):95.

Klemm, L. M., Pettke, T., and Heinrich, C. A. (2008). Fluid and source magma evolution of the Questa porphyry Mo deposit, New Mexico, USA. *Mineralium Deposita*, 43(5):533.

Klemm, L. M., Pettke, T., Heinrich, C. A., and Campos, E. (2007). Hydrothermal evolution of the El Teniente deposit, Chile: Porphyry Cu-Mo ore deposition from low-salinity magmatic fluids. *Economic Geology*, 102(6):1021–1045.

Lamy-Chappuis, B., Heinrich, C. A., Driesner, T., and Weis, P. (2020). Mechanisms and patterns of magmatic fluid transport in cooling hydrous intrusions. *Earth and Planetary Science Letters*, 535:116111.

Landtwing, M. R., Furrer, C., Redmond, P. B., Pettke, T., Guillong, M., and Heinrich, C. A. (2010). The Bingham Canyon porphyry Cu-Mo-Au deposit. III. Zoned copper-gold ore deposition by magmatic vapor expansion. *Economic Geology*, 105(1):91–118.

Lee, C.-T. A. and Morton, D. M. (2015). High silica granites: Terminal porosity and crystal settling in shallow magma chambers. *Earth and Planetary Science Letters*, 409:23–31.

Lerchbaumer, L. and Audétat, A. (2012). High Cu concentrations in vapor-type fluid inclusions: An artifact? *Geochimica et Cosmochimica Acta*, 88:255–274.

Li, N., Ulrich, T., Chen, Y.-J., Thomsen, T. B., Pease, V., and Pirajno, F. (2012). Fluid evolution of the Yuchiling porphyry Mo deposit, East Qinling, China. *Ore Geology Reviews*, 48:442–459.

Lowenstern, J. B. (1995). Applications of silicate melt inclusions to the study of magmatic volatiles. In Thompson, J. F. H., editor, *Magmas, Fluids and Ore Deposits*, volume 23 of *Mineralogical Association of Canada Short Course*, pages 71–99.

Mahood, G. A. (1990). Second reply to comment of RSJ Sparks, HE Huppert and CJN Wilson on'Evidence for long residence times of rhyolitic magma in the Long Valley magmatic system: The isotopic record in the precaldera lavas of Glass Mountain'. *Earth and Planetary Science Letters*, 99(4):395–399.

Malfait, W. J., Seifert, R., Petitgirard, S., Perrillat, J.-P., Mezouar, M., Ota, T., Nakamura, E., Lerch, P., and Sanchez-Valle, C. (2014). Supervolcano eruptions driven by melt buoyancy in large silicic magma chambers. *Nature Geoscience*, 7(2):122.

Marini, L., Principe, C., Chiodini, G., Cioni, R., Fytikas, M., and Marinelli, G. (1993). Hydrothermal eruptions of Nisyros (Dodecanese, Greece). Past events and present hazard. *Journal of Volcanology and Geothermal Research*, 56(1-2):71–94.

Matsuda, J.-i., Senoh, K., Maruoka, T., Sato, H., and Mitropoulos, P. (1999). K-Ar ages of the Aegean volcanic rocks and their implication for the arc-trench system. *Geochemical Journal*, 33(6):369–377.

Mavrogenes, J. A. and Bodnar, R. J. (1994). Hydrogen movement into and out of fluid inclusions in quartz: Experimental evidence and geologic implications. *Geochimica et Cosmochimica Acta*, 58(1):141–148.

Meier, T., Rische, M., Endrun, B., Vafidis, A., and Harjes, H.-P. (2004). Seismicity of the Hellenic subduction zone in the area of western and central Crete observed by temporary local seismic networks. *Tectonophysics*, 383(3-4):149–169.

Mitropolous, P., Tarney, J., Saunders, A. D., and Marsh, N. G. (1987). Petrogenesis of Cenezoic volcanic rocks from the Aegean island arc. *Journal of Volcanology and Geothermal Research*, 32(1-3):177–193.

Nomikou, P. (2004). *Geodynamic of Dodecanise Islands: Kos and Nisyros Volcanic Field*. PhD thesis, University of Athens.

Nomikou, P., Papanikolaou, D., and Dietrich, V. J. (2018). Geodynamics and volcanism in the Kos-Yali-Nisyros volcanic field. In Dietrich, V. J. and Lagios, E., editors, *Nisyros Volcano: The Kos - Yali - Nisyros Volcanic Field*, Active Volcanoes of the World, pages 13–55. Springer International Publishing, Cham.

Oppenheimer, C. (2003). *Volcanic Degassing*, volume 213 of *Geological Society Special Publication*. Geological Society, London.

Papadopoulos, G. A., Sachpazi, M., Panopoulou, G., and Stavrakakis, G. (1998). The volcano-seismic crisis of 1996-97 in Nisyros, SE Aegean Sea, Greece. *Terra Nova*, 10:151–154.

Papazachos, B. C. and Comninakis, P. E. (1971). Geophysical and tectonic features of the Aegean Arc. *Journal of Geophysical Research (1896-1977)*, 76(35):8517–8533.

Papazachos, B. C., Dimitriadis, S. T., Panagiotopoulos, D. G., Papazachos, C. B., and Papadimitriou, E. E. (2005). Deep structure and active tectonics of the southern Aegean volcanic arc. In Fytikas, M. and Vougioukalakis, G. E., editors, *Developments in Volcanology*, volume 7 of *The South Aegean Active Volcanic Arc*, pages 47–64. Elsevier.

Parmigiani, A., Degruyter, W., Leclaire, S., Huber, C., and Bachmann, O. (2017). The mechanics of shallow magma reservoir outgassing. *Geochemistry, Geophysics, Geosystems*, 18(8):2887–2905.

Parmigiani, A., Huber, C., and Bachmann, O. (2014). Mush microphysics and the reactivation of crystal-rich magma reservoirs. *Journal of Geophysical Research: Solid Earth*, 119(8):6308–6322.

Pe-Piper, G., Piper, D. J., and Perissoratis, C. (2005). Neotectonics and the Kos Plateau Tuff eruption of 161 ka, South Aegean arc. *Journal of Volcanology and Geothermal Research*, 139(3-4):315–338.

Pêcher, A. and Boullier, A.-M. (1984). Evolution à pression et température élevées d'inclusions fluides dans un quartz synthétique. *Bulletin de Minéralogie*, 107(2):139–153.

Pettke, T., Oberli, F., Audétat, A., Guillong, M., Simon, A. C., Hanley, J. J., and Klemm, L. M. (2012). Recent developments in element concentration and isotope ratio analysis of individual fluid inclusions by laser ablation single and multiple collector ICP-MS. *Ore Geology Reviews*, 44:10–38.

Pokrovski, G. S., Borisova, A. Y., and Bychkov, A. Y. (2013). Speciation and transport of metals and metalloids in geological vapors. *Reviews in Mineralogy and Geochemistry*, 76(1):165–218.

Pokrovski, G. S., Borisova, A. Y., and Harrichoury, J.-C. (2008). The effect of sulfur on vapor–liquid fractionation of metals in hydrothermal systems. *Earth and Planetary Science Letters*, 266(3):345–362.

Popa, R.-G., Bachmann, O., Ellis, B. S., Degruyter, W., Tollan, P., and Kyriakopoulos, K. (2019). A connection between magma chamber processes and eruptive styles revealed at Nisyros-Yali volcano (Greece). *Journal of Volcanology and Geothermal Research*, 387:106666.

Rauchenstein-Martinek, K., Wagner, T., Wälle, M., and Heinrich, C. A. (2014). Gold concentrations in metamorphic fluids: A LA-ICPMS study of fluid inclusions from the Alpine orogenic belt. *Chemical Geology*, 385:70–83.

Roedder, E. (1984). *Fluid Inclusions*. Walter de Gruyter GmbH & Co KG.

Roedder, E. and Coombs, D. S. (1967). Immiscibility in granitic melts, indicated by fluid inclusions in ejected granitic blocks from Ascension Island. *Journal of Petrology*, 8(3):417–451.

Rohrlach, B. D. and Loucks, R. R. (2005). Multi-million-year cyclic ramp-up of volatiles in a lower crustal magma reservoir trapped below the Tampakan copper-gold deposit by Mio-Pliocene crustal compression in the southern Philippines. In Porter, T. M., editor, *Super Porphyry Copper and Gold Deposits: A Global Perspective*, volume 2, pages 369–407. PGC Publishing, Adelaide.

Rubin, A. M. (1995). Propagation of magma-filled cracks. *Annual Review of Earth and Planetary Sciences*, 23(1):287–336.

Rusk, B. (2012). Cathodoluminescent textures and trace elements in hydrothermal quartz. In Götze, J. and Möckel, R., editors, *Quartz: Deposits, Mineralogy and Analytics*, Springer Geology, pages 307–329. Springer, Berlin, Heidelberg.

Rusk, B. G., Reed, M. H., and Dilles, J. H. (2008). Fluid inclusion evidence for magmatic-hydrothermal fluid evolution in the porphyry copper-molybdenum deposit at Butte, Montana. *Economic Geology*, 103(2):307–334.

Rusk, B. G., Reed, M. H., Dilles, J. H., Klemm, L. M., and Heinrich, C. A. (2004). Compositions of magmatic hydrothermal fluids determined by LA-ICP-MS of fluid inclusions from the porphyry copper–molybdenum deposit at Butte, MT. *Chemical Geology*, 210(1):173–199.

Schatz, O. J., Dolejš, D., Stix, J., Williams-Jones, A. E., and Layne, G. D. (2004). Partitioning of boron among melt, brine and vapor in the system haplogranite–H_2O–NaCl at 800 °C and 100 MPa. *Chemical Geology*, 210(1):135–147.

Schlöglova, K., Wälle, M., and Heinrich, C. A. (2017). LA-ICP-MS analysis of fluid inclusions: Contamination effects challenging micro-analysis of elements close to their detection limit. *Journal of analytical atomic spectrometry*, 32(5):1052–1063.

Schmidt, C., Romer, R. L., Wohlgemuth-Ueberwasser, C. C., and Appelt, O. (2020). Partitioning of Sn and W between granitic melt and aqueous fluid. *Ore Geology Reviews*, 117:103263.

Seo, J. H., Guillong, M., Aerts, M., Zajacz, Z., and Heinrich, C. A. (2011). Microanalysis of S, Cl, and Br in fluid inclusions by LA–ICP-MS. *Chemical Geology*, 284(1-2):35–44.

Seo, J. H. and Heinrich, C. A. (2013). Selective copper diffusion into quartz-hosted vapor inclusions: Evidence from other host minerals, driving forces, and consequences for Cu–Au ore formation. *Geochimica et Cosmochimica Acta*, 113:60–69.

Severs, M. J., Azbej, T., Thomas, J. B., Mandeville, C. W., and Bodnar, R. J. (2007). Experimental determination of H2O loss from melt inclusions during laboratory heating: Evidence from Raman spectroscopy. *Chemical Geology*, 237(3-4):358–371.

Shimizu, A., Sumino, H., Nagao, K., Notsu, K., and Mitropoulos, P. (2005). Variation in noble gas isotopic composition of gas samples from the Aegean arc, Greece. *Journal of Volcanology and Geothermal Research*, 140(4):321–339.

Shinohara, H. (2008). Excess degassing from volcanoes and its role on eruptive and intrusive activity. *Reviews of Geophysics*, 46(4).

Shinohara, H., Kazahaya, K., and Lowenstern, J. B. (1995). Volatile transport in a convecting magma column: Implications for porphyry Mo mineralization. *Geology*, 23(12):1091–1094.

Sillitoe, R. H. (1973). The tops and bottoms of porphyry copper deposits. *Economic Geology*, 68(6):799–815.

Sillitoe, R. H. (2010). Porphyry copper systems. *Economic geology*, 105(1):3–41.

Smith, P. E., York, D., Chen, Y., and Evensen, N. M. (1996). Single crystal 40Ar-39Ar dating of a Late Quaternary paroxysm on Kos, Greece: Concordance of terrestrial and marine ages. *Geophysical Research Letters*, 23(21):3047–3050.

Sodoudi, F., Kind, R., Hatzfeld, D., Priestley, K., Hanka, W., Wylegalla, K., Stavrakakis, G., Vafidis, A., Harjes, H.-P., and Bohnhoff, M. (2006). Lithospheric structure of the Aegean obtained from P and S receiver functions. *Journal of Geophysical Research: Solid Earth*, 111(B12).

Sourirajan, S. and Kennedy, G. C. (1962). The system H2O-NaCl at elevated temperatures and pressures. *American Journal of Science*, 260(2):115–141.

Steele-MacInnis, M., Lecumberri-Sanchez, P., and Bodnar, R. J. (2012). Short note: HokieFlincs_H2O-NaCl: A Microsoft Excel spreadsheet for interpreting microthermometric data from fluid inclusions based on the PVTX properties of H2O-NaCl. *Computers & Geosciences*, 49:334–337.

Stefanova, E., Driesner, T., Zajacz, Z., Heinrich, C. A., Petrov, P., and Vasilev, Z. (2014). Melt and fluid inclusions in hydrothermal veins: The magmatic to hydrothermal evolution of the Elatsite porphyry Cu-Au deposit, Bulgaria. *Economic Geology*, 109(5):1359–1381.

Student, J. J. and Bodnar, R. J. (1999). Synthetic fluid inclusions XIV: Coexisting silicate melt and aqueous fluid inclusions in the haplogranite–H2O–NaCl–KCl system. *Journal of Petrology*, 40(10):1509–1525.

Sun, S.-S. and McDonough, W. F. (1989). Chemical and isotopic systematics of oceanic basalts: Implications for mantle composition and processes. *Geological Society, London, Special Publications*, 42(1):313–345.

Symonds, R. B., Gerlach, T. M., and Reed, M. H. (2001). Magmatic gas scrubbing: Implications for volcano monitoring. *Journal of Volcanology and Geothermal Research*, 108(1):303–341.

Tattitch, B. C. and Blundy, J. D. (2017). Cu-Mo partitioning between felsic melts and saline-aqueous fluids as a function of XNaCleq, fO2, and fS2. *American Mineralogist*, 102(10):1987–2006.

Tramontano, S., Gualda, G. A., and Ghiorso, M. S. (2017). Internal triggering of volcanic eruptions: Tracking overpressure regimes for giant magma bodies. *Earth and Planetary Science Letters*, 472:142–151.

Ulrich, T., Günther, D., and Heinrich, C. A. (2002). The evolution of a porphyry Cu-Au deposit, based on LA-ICP-MS analysis of fluid inclusions: Bajo de la Alumbrera, Argentina. *Economic Geology*, 97(8):1889–1920.

van Hinsbergen, D. J. and Boekhout, F. (2009). Neogene brittle detachment faulting on Kos (E Greece): Implications for a southern break-away fault of the Menderes metamorphic core complex (western Turkey). *Geological Society, London, Special Publications*, 311(1):311–320.

Vanko, D. A., Bodnar, R. J., and Sterner, S. M. (1988). Synthetic fluid inclusions: VIII. Vapor-saturated halite solubility in part of the system NaCl-CaCl2-H2O, with application to fluid inclusions from oceanic hydrothermal systems. *Geochimica et Cosmochimica Acta*, 52(10):2451–2456.

Varshneya, A. K., Cooper, A. R., and Cable, M. (1966). Changes in composition during electron micro-probe analysis of K2O–SrO–SiO2 glass. *Journal of Applied Physics*, 37(5):2199–2199.

Veksler, I. V. (2004). Liquid immiscibility and its role at the magmatic–hydrothermal transition: A summary of experimental studies. *Chemical Geology*, 210(1-4):7–31.

Vityk, M. O. and Bodnar, R. J. (1995). Textural evolution of synthetic fluid inclusions in quartz during reequilibration, with applications to tectonic reconstruction. *Contributions to Mineralogy and Petrology*, 121(3):309–323.

Voegelin, A. R., Pettke, T., Greber, N. D., von Niederhäusern, B., and Nägler, T. F. (2014). Magma differentiation fractionates Mo isotope ratios: Evidence from the Kos Plateau Tuff (Aegean Arc). *Lithos*, 190:440–448.

Vougioukalakis, G. E., Satow, C. S., and Druitt, T. H. (2019). Volcanism of the South Aegean Volcanic Arc. *Elements*, 15(3):159–164.

Wark, D. A. and Watson, E. B. (2006). TitaniQ: A titanium-in-quartz geothermometer. *Contributions to Mineralogy and Petrology*, 152(6):743–754.

Webster, J. D. (2004). The exsolution of magmatic hydrosaline chloride liquids. *Chemical Geology*, 210(1-4):33–48.

Willmann, R. (1983). Neogen und jungtertiäre Entwicklung der Insel Kos (Ägäis, Griechenland). *Geologische Rundschau*, 72(3):815–860.

Wilson, L. (1976). Explosive volcanic eruptions—III. Plinian eruption columns. *Geophysical Journal International*, 45(3):543–556.

Zajacz, Z., Halter, W. E., Pettke, T., and Guillong, M. (2008). Determination of fluid/melt partition coefficients by LA-ICPMS analysis of co-existing fluid and silicate melt inclusions: Controls on element partitioning. *Geochimica et Cosmochimica Acta*, 72(8):2169–2197.

Zajacz, Z., Hanley, J. J., Heinrich, C. A., Halter, W. E., and Guillong, M. (2009). Diffusive reequilibration of quartz-hosted silicate melt and fluid inclusions: Are all metal concentrations unmodified? *Geochimica et Cosmochimica Acta*, 73(10):3013–3027.

Zeng, L., Bao, Z., Shan, Q., Yang, W., Zhao, Y., and Li, N. (2016). Magmatic–hydrothermal evolution of highly fractionated granites: Evidence from the Kuiqi miarolite in Fujian province, SE China. *Journal of Asian Earth Sciences*, 123:100–110.

Zhang, D. and Audétat, A. (2017). What caused the formation of the giant Bingham Canyon porphyry Cu-Mo-Au deposit? Insights from melt inclusions and magmatic sulfides. *Economic Geology*, 112(2):221–244.

Zhang, P., Zhang, L., Wang, Z., Li, W.-C., Guo, X., and Ni, H. (2018). Diffusion of molybdenum and tungsten in anhydrous and hydrous granitic melts. *American Mineralogist*, 103(12):1966–1974.

Zouzias, D. and St. Seymour, K. (2008). Consanguineous geochemistry of the Kos Plateau and Tilos D and E Pumices, Aegean Volcanic Arc, Hellas. *Neues Jahrbuch für Mineralogie - Abhandlungen*, pages 231–241.